The Influence of Dielectric Constant of Polymer Donors and Their Blends on the Performance of Organic Solar Cells

by

Pankaj Kumar

A thesis
presented to the University of Waterloo
in fulfillment of the
thesis requirement for the degree of
Master of Applied Science
in
Chemical Engineering

Waterloo, Ontario, Canada, 2021

AUTHOR'S DECLARATION

I hereby declare that I am the sole author of this thesis. This is a true copy of the thesis, including any required final revisions, as accepted by my examiners.
I understand that my thesis may be made electronically available to the public.

Abstract

Organic solar cell (OSC) is a promising photovoltaic technology because the optoelectronic properties of the organic materials can be easily tuned, which allows for constant improvement in the device performance, material cost, and processability. Although significant progress has been made and power conversion efficiency (PCE) of over 18% has been achieved, there is still room for improvement and for potentially bridging the gap between organic and inorganic solar cells in terms of efficiency. For example, the low dielectric constant of polymer donors used in the active layer of the OSC leads to the formation of tightly bound excitons (electron-hole pairs still under Coulombic attraction) which might lead to high exciton binding energies (E_b), thus increasing the recombination losses and lowering the overall device performance. However, enough attention has not been paid to the role of the dielectric constant of the neat polymer films and their blends with non-fullerene acceptors in OSC devices.

In this study, the exciton binding energies of six polymer donors (three commercial and three synthesized in our lab) are measured using photoconductivity quantum efficiency measurement. Then, the dielectric constants (ε_r) of these polymers are measured to explore their relationship with the E_b. A lack of correlation between ε_r and E_b was found and therefore, suggesting that increasing the dielectric constant (using fluorination, etc.) need not necessarily decrease the E_b of polymer donors. After studying the effects of molecular structure on the measured ε_r and E_b, the effects of (i) processing conditions (thermal annealing and addition of 1,8-diiodooctane (DIO) additive in blends), and (ii) dielectric constant of donor polymers, on the blend dielectric constants were investigated. The changes in V_{OC} and FF have been mainly focused on since they are directly influenced by the donor/acceptor material properties (specifically, E_b and ε_r) and the changes in active layer morphology. It is found that the effect of processing conditions on the dielectric constants of blends is minimal. Moreover, increasing the dielectric constant of the polymer donor and non-fullerene acceptor, might not necessarily lead to an increased dielectric constant of the blend, and small changes in dielectric constants do not show visible effects on the device performance parameters.

Acknowledgements

I would like to sincerely thank my supervisor, Dr. Yuning Li, who offered me the opportunity to work on this topic and for the constant guidance, support, and encouragement throughout. In addition, I acknowledge the excellent atmosphere provided by the extraordinary lab management and work ethics in the group.

I am obliged especially to Dr. Keqiang He and Yi Yuan for providing me high performance materials for my experiments.

I wish to thank Zhifang Zhang and Dr. Arthur Hendsbee for the excellent discussions and for helping me feel comfortable after arrival in the group.

Many thanks to Prof. Jean Duhamel's group for accommodating me in their lab for photoluminescence quenching measurements of thin films.

I am thankful to my colleagues, especially Jenner Ngai, Chenyang Guo, Wuqi Li, Xiguang Gao, and Zhong Ma, for all the wonderful times together.

Finally, I would like to thank my family and friends for their constant support.

Table of Contents

List of Figures

List of Tables

Chapter 1
Introduction

1.1 Introduction to organic photovoltaics

Organic photovoltaics (OPVs) as a renewable energy source has been studied extensively during the past decade. The intrinsic advantages of this thin-film technology over the inorganic solar cell technologies (such as ease of processability, flexible substrate design, and potential low-cost roll-to-roll (R2R) printing) have prompted an intensive focus on the development of novel materials and device design. As a result, the efficiency of organic solar cells has reached a remarkable 18%[1], establishing OPV devices as promising alternatives to inorganic solar cells for commercial applications.[2,3]

Although substantial success has been achieved towards improving the efficiency of OPVs and the gap between organic and inorganic solar cell technologies (such as Si, CIGS, and perovskite solar cells)[4] seems to be narrowing, there is still room for improvement. There are several types of loss mechanisms that limit the achievable power conversion efficiency (PCE) below the theoretical Shockley and Queisser[5] limit of 33.7%, achievable with a semiconductor having a bandgap of 1.34 eV. Even in a conservative estimate, Hou et al.[6] predicted that a PCE of > 20% for OSCs can be obtained if voltage loss (V_{loss}) can be lowered to < 0.45 V. For high PCE perovskites, V_{loss} of 0.3 V has been reported,[7] while the current state-of-the-art organic solar cells show V_{loss} of ca. 0.6 V.[8,9] Understanding the mechanisms for V_{loss} and hence providing guidelines for designing new materials for the active layer of the organic solar cell device remains an active area of research. Increasing fill factor (FF) is another direction where the focus has been increasing. The FFs of state-of-the-art OSCs are still much lower than those of the inorganic solar cells (fill factor and voltage loss is defined in the subsequent sections).

1.2 Theory of organic solar cells

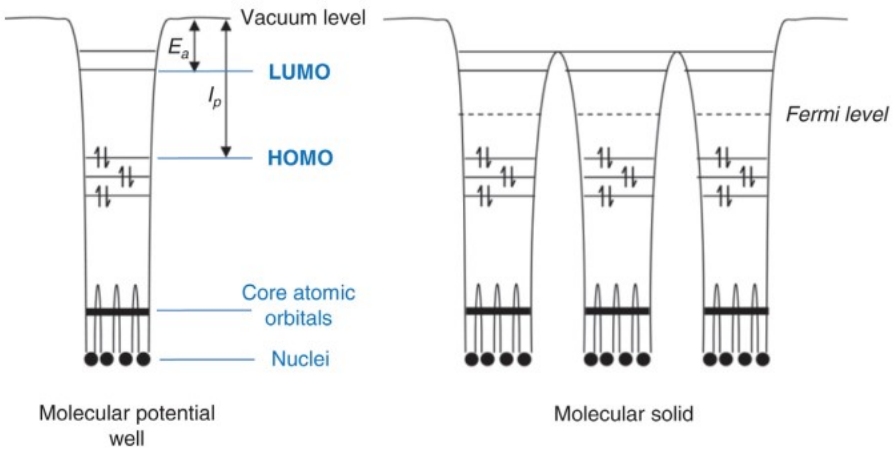

Figure 1 Schematic diagram illustrating the potential well for an isolated molecule (left) and an aggregation of molecules (right) held together by van der Waals interactions. Adapted from Gregg, 2003.[11]

The mechanism of working of organic solar cells is fundamentally different from the conventional inorganic solar cells, such as silicon photovoltaics. The continuous and strongly bound lattice (due to *covalent bonds*) in inorganic semiconductors ensure that the charge carriers are *delocalized* and the Coulombic force of attraction between holes and electrons is very small. Moreover, due to the presence of a high dielectric constant, the binding energy of photogenerated electrons and holes is much smaller than the thermal energy of charge carriers at room temperature (~26 meV). Therefore, absorption of a photon of light with enough energy results directly in free electrons and holes, which can be swept across the built-in potential of the p-n junction at the interface between p and n-doped silicon.

In contrast, the absorption of a photon in organic semiconductors does not result in free electron and hole due to the presence of large Coulombic attraction (0.2-1 eV).[10–12] This large Coulomb interaction (binding energy) is a consequence of the electronic structure of organic

semiconductors. The highest occupied molecular orbital (HOMO) and lowest unoccupied molecular orbital (LUMO) (analogous to conduction and valence band in inorganic semiconductors) of organic semiconductors are coupled weakly due to the presence of *van der Waals-type* forces. These weakly interacting energy levels of individuals molecules are highly *localized* and therefore organic semiconductor is also called molecular solid (illustrated in **Figure 1**).[13]

1.2.1 **Operation of photovoltaic solar cells**

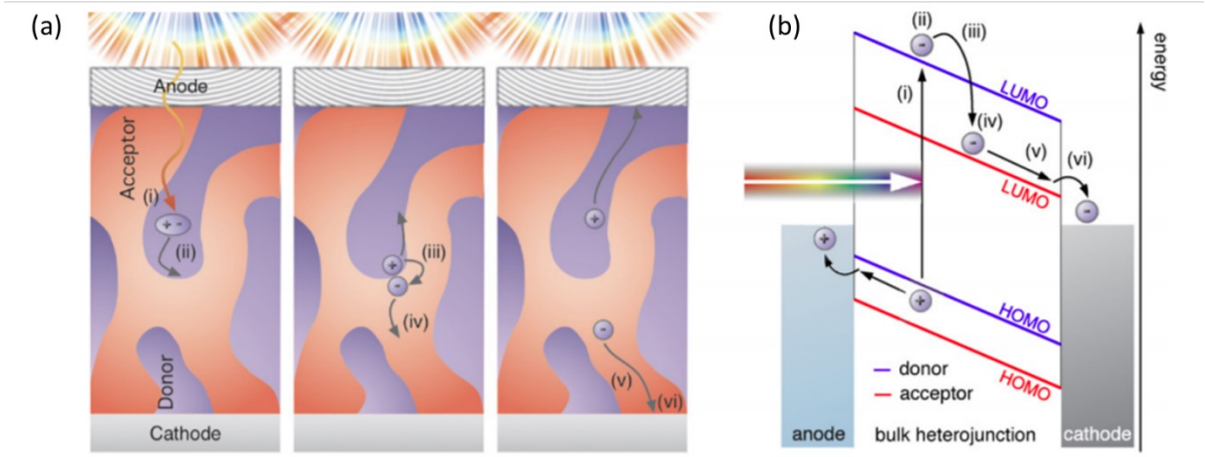

Figure 2 (a) Steps in the photovoltaic processes in OSC: (i) Exciton generation from absorbed photon in donor; (ii) exciton diffusion to donor:acceptor interface; (iii) exciton dissociation by electron transfer to acceptor; (iv) separation of still coulombically bound electron-hole pair due to electric field; (v) charge transport of electron and holes (competing with recombination); and (vi) extraction of charges. (b) Energy diagram- simplified version. Adapted from Carsten Deibel and Vladimir Dyakonov, 2010.[15]

An organic solar cell (OSC) works on the principle of direct conversion of incident sunlight (photon with energy hυ, h= plank constant, υ= frequency) into electrical energy. As the photon

is absorbed, an electrically bound hole-electron pair (exciton) is generated, which dissociates into free carriers under the influence of a built-in electric field (due to local electric field created by LUMO or HOMO energy level offsets and also contributed by work function difference of the electrodes).[14] These free charges are conducted to their respective electrodes because of the preferred mobility of donor (to conducts holes) and acceptor (to conducts electrons). All these steps and relevant energy levels are shown in **Figure 2** (adapted from Carsten Deibel and Vladimir Dyakonov[15]). The driving forces to make this happen are internal built-in electric fields (V_{bi}) arising due to the difference in the electrode work functions and concentration gradients of charge carriers.[16–20] It is possible that the electron-hole pair combine before separating at the donor:acceptor interface and this recombination is termed geminate recombination. The recombination loss can still take place after separation into free carriers when the separated electrons/holes can randomly meet holes/electrons within the blend active layer and this recombination is called non-geminate recombination.[21]

The selective transport (or minimization of recombination loss) is enhanced by the interface/buffer layers, which selectively conduct/block one of the carriers. For efficient charge collection, anode and cathode materials should be chosen such that they form Ohmic contacts (without barrier) for the transport of holes and electrons, respectively. The interface layer is introduced to achieve the required energy level matching.[22]

A typical solar cell (either conventional or inverted architecture as shown in **Figure 3**) consists of:

- A transparent bottom electrode: ITO is the most common bottom electrode in lab level small devices. Other choices include Ag nanowires or highly conductive PEDOT:PSS, which are more relevant to R2R applications.
- A hole transport layer: Depending on the type of material used, HTL can either act as blocking electrons or selectively conducting holes, or forming an interface dipole that increases the barrier for electron transport.
- A polymer blend of donor and acceptor: The active layer consists of electron donor and electron acceptor material. In a bulk heterojunction device (BHJ), donor and acceptor

are intimately mixed to achieve a nanoscale morphology. The chemical structures of some of the donor polymers and non-fullerene acceptors (NFAs) are shown in **Figure 5**.

- An electron transport layer: Electron transport layer functions the opposite of HTL. The high conductivity and preferential hole blocking/electron-conducting nature of ETL determines the motion of the electron in opposite direction to the hole.
- A top electrode: The top electrode may or may not be semitransparent. The function of this contact is to collect electrons in normal device structure and holes in inverted structure.

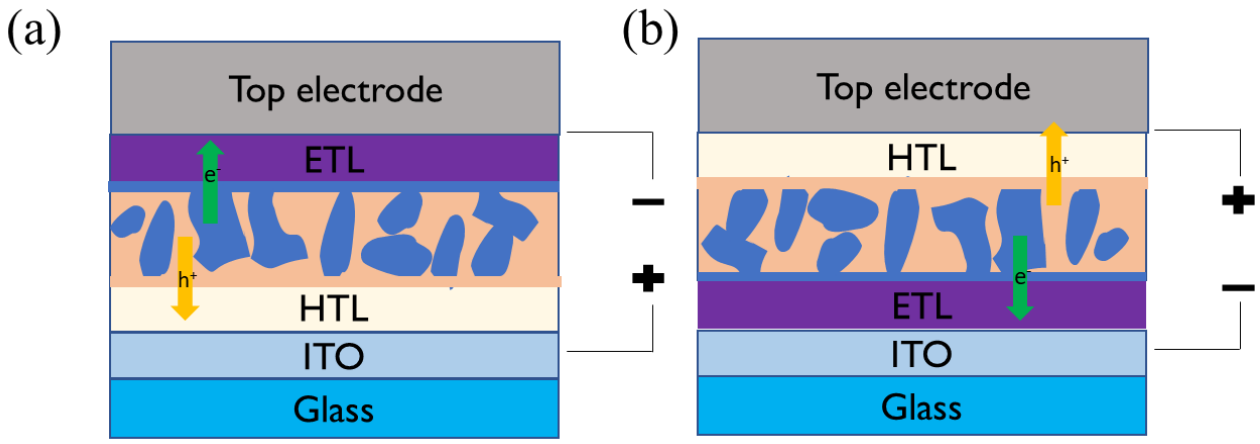

Figure 3 Schematic diagram for (a) conventional and (b) inverted OSC device structure. Electron transporting layer (ETL) and hole transport layer (HTL) ease the extraction of charges at cathode and anode, respectively. The arrows show the direction of electron and hole transport after charge separation in bulk heterojunction blend of donor and acceptor.

The performance of a solar cell is characterized using a voltage sweep of current density (J-V). A typical J-V curve is shown in **Figure 4**. The curve in turn is described by the following equations in the dark and under illumination (illumination source simulates the solar spectrum at AM1.5G standard with an intensity of 1000 W m^{-2}):

$$J(V) = J_o\left[exp\left[\frac{eV}{nkT}\right] - 1\right] \quad 1.1$$

$$J(V) = J_o\left[exp\left[\frac{eV}{nkT}\right] - 1\right] + J_{ph} \quad 1.2$$

where J_o is the reverse dark current, V is the bias voltage, n is the diode quality factor, k is the Boltzmann constant and T is the temperature.[23] The power conversion efficiency (PCE) is determined using the equations at input light intensity of 100 mW cm^{-2} (P_{in}).

$$FF = \frac{P_{max}}{AJ_{sc}V_{oc}} \quad 1.3$$

$$PCE = \frac{J_{sc}V_{oc}FF}{P_{in}} \quad 1.4$$

The open circuit voltage (V_{OC}) is defined as the maximum voltage that is obtained at zero current flowing through the device. The short circuit current density (J_{sc}) is the maximum current density at no applied bias. The fill factor is the ratio of the maximum operating power output from the device (P_{max}) to the input power. Thus, the power conversion efficiency is the ratio of the maximum operating power (P_{max}) to the input power of the incident light on the solar cell (P_{in}).

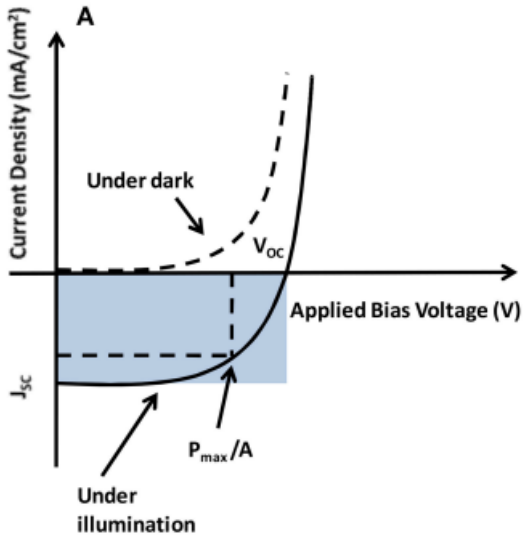

Figure 4 A typical solar cell current voltage characteristic.

These parameters are directly related to the properties of the materials used, the morphology of the active layer, and interfaces present in the device. J_{sc} is dependent on the absorption spectrum of the materials used in the active layer. V_{oc} is linearly related to the difference in the $LUMO_A$ and $HOMO_D$. A low-lying HOMO (obtained through structure modification) of the donor will lead to high V_{OC}. Another feasible way is to increase the dielectric constant of the donor (and/or acceptor) which can reduce the exciton binding energy, and thus reducing the required donor-acceptor offset ΔLUMO for exciton dissociation, achieving a higher V_{OC}.[24,25] FF reflects the shunt (R_{sh}) and series (R_s) resistances and quality of the diode (represented by an ideality factor, n)[26,27] present in the device. Overall, these parameters depend on the material properties of the active layer. High and balanced hole (μ_h) and electron (μ_e) mobilities of $>10^{-4}$ cm^2 V^{-1} s^{-1} in blend films are usually required to achieve a high FF.

1.3 Characterization tools and methods

In a bulk heterojunction (BHJ) solar cell, where the blend active layer is composed of donor and acceptor materials with complementary properties, it becomes increasingly important to characterize some fundamental material properties, before selecting a particular combination of donor and acceptor. A "matching" donor:acceptor combination is required for high performance BHJ organic solar cells. Some of these characterization methods are listed here:

1.3.1 **Cyclic voltammetry**

Cyclic voltammetry (CV) determines the oxidative and reductive potentials of active layer materials. The experiment is carried out using an electrochemical analyzer, where the materials to be tested are cast on a platinum working electrode disc as a thin film. 0.1 M tetrabutylammonium hexafluorophosphate (Bu_4NPF_6) solution in acetonitrile is used as the electrolyte and a current-voltage sweep is carried out at a scan rate of 50 mV s^{-1}. Ferrocene is used as the internal standard with the HOMO level of ferrocene assumed to be -4.80 eV. Silver/silver chloride is used as the reference electrode and another platinum electrode disc is used as the auxiliary electrode. The measurable change in current for the sample would be calculated with respect to the oxidative potential of ferrocene. The HOMO and LUMO of the samples are then estimated from the cyclic voltammograms while accounting for the Ferrocene oxidation potential.[28]

1.3.2 **UV-Vis-NIR spectroscopy**

UV-Vis-NIR spectroscopy is used to obtain the bandgap of the donor or acceptor using the absorption onset wavelength in thin films. Additionally, the packing behavior of the thin neat and blends films can also be analyzed by observing the red/blue shift of absorption onsets and peaks.

1.3.3 **Photoluminescence quenching characterization**

Photoinduced charge transfer efficiency (from donor to acceptor or vice versa), which is a key step in the OSC operation, can be probed via photoluminescence (PL) quenching and PL decay measurements of the blend films relative to the neat films.[29,30] For a donor:acceptor blend

with sufficient ΔHOMO and ΔLUMO offsets, PL quenching is very sensitive to morphology (donor and acceptor domain sizes in the blend are dictated by miscibility and film formation kinetics[31]) of the active layer. High miscibility might lead to a high PL quenching efficiency (PLQE), but it would retard the charge collection process by decreasing the electron and hole mobilities due to lack of percolating path to the electrodes.[31–35] Therefore, PLQE measurements in combination with electron/hole mobility measurement (discussed in section 1.3.5) can shine light on the balance between miscibility and domain (donor/acceptor) purity, in the active layer blend.

1.3.4 **External quantum efficiency measurement**

The external quantum efficiency (EQE) is the ratio of the number of carriers collected by the solar cell to the number of photons of a particular wavelength incident on the solar cell.

1.3.5 **SCLC mobility measurement**

For mobility measurement using the space charge limited current (SCLC) method, a hole-only or electron-only diode device structure is used, where at least one electrode must efficiently inject one type of carriers (either electron or hole), while the other electrode should block injection of charge carriers of the opposite polarity. When a voltage is applied to the diode, a unipolar charge is injected into the active layer film, resulting in a build-up of space-charge.[36]

In this thesis, the SCLC hole mobility is measured in hole-only devices, employing a device architecture of ITO/PEDOT:PSS/active layer/MoO_x/Ag, while the SCLC electron mobility is measured using a device architecture ITO/ZnO/active layer/LiF/Al. In these device structures, PEDOT:PSS/MoO_x and ZnO/LiF help in the formation of ohmic contacts at the contacts. The obtained J-V curve is used to fit the Mott-Gurney equation:[37]

$$J_{sclc} = \frac{9}{8}\,\mu\varepsilon\,\frac{V_{appl}^2}{d^3} \qquad 1.5$$

where $\varepsilon = \varepsilon_o\varepsilon_r$, ε_o is the permittivity of vacuum free space, ε_r is the relative permittivity (dielectric constant) of the material, μ is the SCLC mobility, V_{appl} is the applied voltage

corrected for work function difference (if any) between the electrodes, and d is the thickness of the film.

1.3.6 **Morphology characterization**

Atomic force microscopy (AFM) characterizes the surface morphology and roughness of the thin film samples, in height and phase imaging mode.

1.3.7 **Dielectric constant (capacitance-frequency) measurement**

Parallel-plate-capacitance measurement using impedance spectroscopy is a straightforward method to calculate the dielectric constant.[38] The active layer is sandwiched between two metallic parallel electrodes and a small perturbation of low amplitude AC signal (10-20 mV) with sweeping through the frequency range of interest (e.g., 100 Hz-1 MHz). The obtained impedance is used to extract the capacitance using[39]:

$$C^* = \frac{1}{j\omega Z^*} = \frac{-Z^{"}}{\omega|Z|^2} + j\frac{-Z'}{\omega|Z|^2} \qquad 1.6$$

where $j^2 = -1$ and Z^* is defined as the impedance complex function indicating impedance value at a particular frequency. Then the dielectric function is derived from:

$$\varepsilon_r^{"}(\omega) = \frac{C^*(\omega)}{C_0} = \varepsilon_r' - j\varepsilon_r^{"} \qquad 1.7$$

where $C_0 = \varepsilon_0 A/d$ is the capacitance of the empty capacitor, $\varepsilon_0 = 8.85 \times 10^{-12}$ F m^{-1} is the electric permittivity of vacuum, A is the area and d is the thickness. The real part of the dielectric function corresponds to the relative dielectric constant, ε_r, of the material, while the imaginary part encompasses loss mechanisms such as conductance and relaxation processes.

In order to correlate the dielectric constant with the real device performance, the timescales associated with recombination (tens of microseconds) in OSCs are considered which fall in the kHz to MHz frequency range.[40] In addition, a negative bias is often applied to minimize the impact of injected charge carries through injection.[41]

1.3.8 **Built-in potential via Mott-Schottky analysis**

In OSCs, wherein, the exciton diffusion lengths and carrier mobilities are limited, a strong built-in electric field across the active layer is required to enhance the charge extraction rate and decrease the recombination rate.[42] This built-in potential V_{bi} (or contact potential) originates primarily due to the work function difference between the anode and cathode contact[42] and the presence of dipole at the contacts.[43]

In organic diodes and solar cells, where the active layers are typically sandwiched between two selective (and usually different) metal electrodes, the work function difference of the electrodes determines V_{bi}, which in turn determines the J-V characteristic of the device. The internal electric field, charge concentration profiles, V_{OC} and hence PCE depends on V_{bi}. In most cases, the maximum V_{OC} achievable is also limited by V_{bi}. It should also be noted that because of charges injected from the contacts near the interface (between contact and active layer), the apparent V_{bi} is generally lower than the actual V_{bi}.[44] Kirchartz et al.[45] suggested that in cases where recombination is only determined by recombination at the internal D:A interface and not at the contacts, the V_{OC} need not depend on the V_{bi}, while the FF drops significantly once the V_{bi} drops below the open-circuit voltage. This theory was recently supported by Duan et al.[46], where, for the same type of device, the decrease in V_{bi} led to inefficient device operation with lower V_{OC}. Han et al.[47] found that the inverted configuration nonfullerene OSCs had a higher built-in potential, compared with a normal OSC prepared using the same blend system, which was favorable for achieving reduced recombination and enhanced charge extraction. Vasilopoulou et al.[43] proposed that an enhanced exciton dissociation can be achieved upon increasing the device's built-in field (due to shift of the work function).[43]

Upama et al.[48] suggested that very high annealing temperature (above the optimum annealing temperature) could induce disorder at the surface (localized states) of the active layer resulting in lower built-in-potential and thus lower FF and poor Voc.

Guerrero et al.[49] studied the coverage of cathode contact with the acceptor molecule ($PC_{70}BM$) in PTB7:$PC_{70}BM$ based device. The effect on V_{bi} and V_{OC} was evident: Voc changes from 0.72 V for the optimum device with DIO additive to 0.78 V (J_{SC} = 14.28 mA cm^{-}

^{2}; FF = 0.69; PCE = 6.69%) in the under-optimized device (without the additive). Meanwhile, V_{bi} values changed from 0.673 V to 1.00 V, respectively. Therefore, the change in V_{bi} can be used as a tool to investigate the change in donor/acceptor coverage of the contacts (since the strength of the dipole and the band bending contribution will greatly depend on the material which is physically present at the interface). The device with 100% fullerene coverage (with D:A ratio 1:6) of the cathode contact corresponded to a V_{bi} of 0.52 V, while that with ~0% coverage corresponded to V_{bi} of 1.30 V. The best performance was seen in a device with 80% fullerene coverage with V_{bi} = 0.673 V.

In this thesis, V_{bi} change would be measured to account for the change in V_{OC} and FF of the studied OSCs, due to changes at the blend active layer/contact interface, thereby excluding the effects from the dielectric constant changes.

Mott-Schottky plot can be used to extract this built-in potential. In the Mott-Schottky plot (C^{-2}-V plot), V_{bi} corresponds to the intercept with the voltage axis.[42]

1.3.9 **Surface energy and miscibility analysis**

Flory−Huggins interaction parameter (χ) can predict the morphology evolution in the active layer.[31] An ideal morphology is neither too pure (leading to low PL quenching of donor and acceptor in blends or low photoinduced charge transfer) nor too mixed (leading to low charge mobilities). The parameter χ can be calculated by the differential scanning calorimetry (DSC) measurements (melting point depression method) or surface energy measurement of donor and acceptor.[31,34,35,50–52] In the surface energy (surface tension) method, a simple relation can be used to probe the relative miscibility of a system of donor and acceptor[53]:

$$\chi \propto \left(\sqrt{\gamma_{donor}} - \sqrt{\gamma_{acceptor}}\right)^2 \qquad 1.8$$

Moreover, the surface tension of the donor and acceptor films can be calculated by Wu's model[54]:

$$\gamma_{water}\,(1+cos\theta_{water}) = \frac{4\gamma^{d}_{water}\,\gamma^{d}}{\gamma^{d}_{water}+\ \gamma^{d}} + \frac{4\gamma^{p}_{water}\gamma^{p}}{\gamma^{p}_{water}+\ \gamma^{p}} \qquad 1.9$$

$$\gamma_{GL}\,(1+cos\theta_{GL}) = \frac{4\gamma^{d}_{GL}+\gamma^{d}}{\gamma^{d}_{GL}+\ \gamma^{d}} + \frac{4\gamma^{p}_{GL}\,\gamma^{p}}{\gamma^{p}_{GL}+\ \gamma^{p}} \qquad 1.10$$

$$\gamma = \gamma^{d} + \gamma^{p} \qquad 1.11$$

where θ is the contact angle of each thin film, and γ is the surface tension of samples, which is equal to the sum of the dispersion (γ^{d}) and polarity (γ^{p}) components; γ_{water} and γ_{GL} are the surface tensions of the water and glycerol (sometimes other liquids such as ethylene glycol EG can be used); and γ^{d}_{water}, γ^{d}_{GL}, γ^{p}_{water}, and γ^{p}_{GL} are the dispersion and polarity components of γ_{water} and γ_{GL}.

1.4 Desirable properties of active layer materials

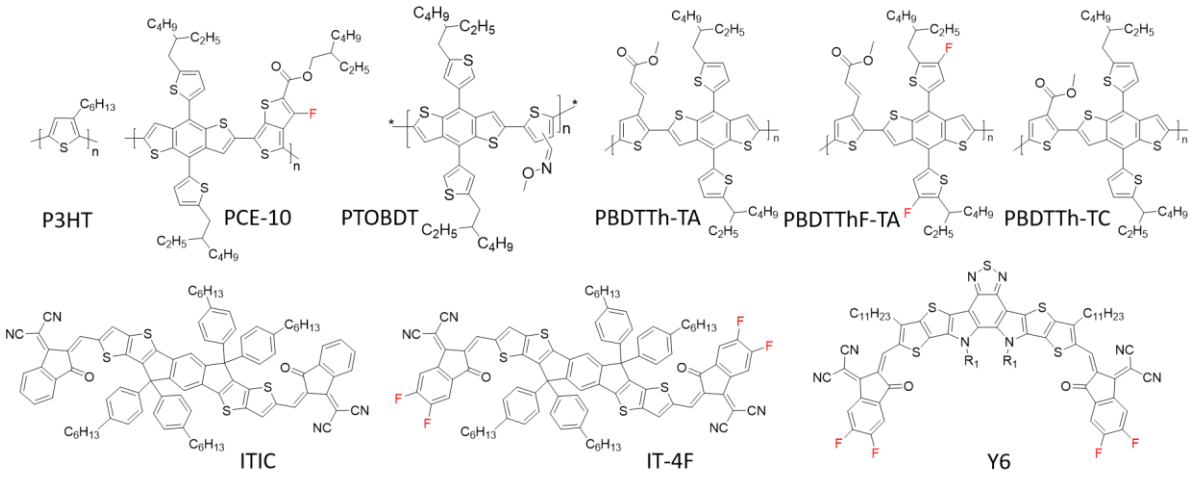

Figure 5 Chemical structures of donors (top row) and non-fullerene acceptors (bottom row), studied in this thesis.

1.4.1 **Matching of properties with the acceptor**

Apart from complementary absorption spectra (determined from the optical band gaps) of donor and acceptor to maximize the photon absorption, a suitable relative energy alignment between donor and acceptor, is another key criterion for selecting a particular combination of donor and acceptor. For example, from the relative alignments for the polymer donors and acceptors are shown in **Figure 6** and **Table 1**, to achieve sufficient ΔHOMO offsets between the donor and acceptors, some combinations can be predicted to be less efficient than the other. PBDTThF-TA:ITIC combination has a ΔHOMO= 0.01 eV, which might lead to low PLQE, although there are a few D:A systems that work without any offsets.[55,56]

Table 1 Optoelectronic properties of materials used in OSC active layer.

	E_g^{opt} (eV)[a]	E_{HOMO} (eV)[b]	E_{LUMO} (eV)[c]
Donors			
P3HT	1.85	-5.05	-3.20
PCE-10	1.58	-5.48	-3.90
PTOBDT	2.03	-5.60	-3.57
PBDTTh-TA	2.00	-5.50	-3.50
PBDTTh-TC	2.03	-5.60	-3.57
PBDTThF-TA	2.02	-5.70	-3.68
Acceptors			
	E_g^{opt} (eV)[a]	E_{HOMO} (eV)[b]	E_{LUMO} (eV)[d]
ITIC	1.59	-5.71	-3.98

IT-4F	1.52	-5.79	-4.13
Y6	1.33	-5.76	-4.11

[a] Obtained from thin film absorption spectra; [b] obtained by $E_{HOMO} = -(4.80 + E_{onset}^{ox})$; [c] obtained by $E_{LUMO} = E_{HOMO} + E_g^{opt}$; [d] obtained from $E_{LUMO} = -(4.80 + E_{onset}^{red})$.

It was an agreed knowledge based on experience with fullerene acceptor based OSCs for a long time that a sufficient energy level offset of ≥ 0.3 eV between donor and acceptor (ΔHOMO or ΔLUMO), is required for efficient charge separation.[14,57–61] This is due to the nature of organic semiconductors that typically have much larger exciton binding energies (~0.3-1 eV) than inorganic semiconductors. However, with the rise of NFAs, several works have demonstrated highly efficient OSCs with efficient and fast charge separation at ΔHOMO (and/or ΔLUMO) values close to 0 eV.[62–65] It should be emphasized that in the majority of the systems, a "certain minimum" driving force is required for balancing the exciton dissociation probability and V_{OC} loss.[55] A larger ΔHOMO, accordingly, can provide sufficient driving force for higher exciton dissociation probability (P_{diss}) and PCE. Although minimizing ΔHOMO can effectively reduce the E_{loss} ($E_{loss} = eV_{loss} = E_g/q - V_{OC}$; where E_g corresponds to the lowest bandgap in the blend), the decreasing driving force will diminish the exciton dissociation process since V_{OC} is proportional to the difference between LUMO of the acceptor and HOMO of the donor.

In summary, some D:A systems work well even with ΔHOMO offsets and some require a certain minimum, and therefore, in cases with low offsets (low driving force for charge separation), the performance of the device will depend on the specific materials used in the D:A blend.

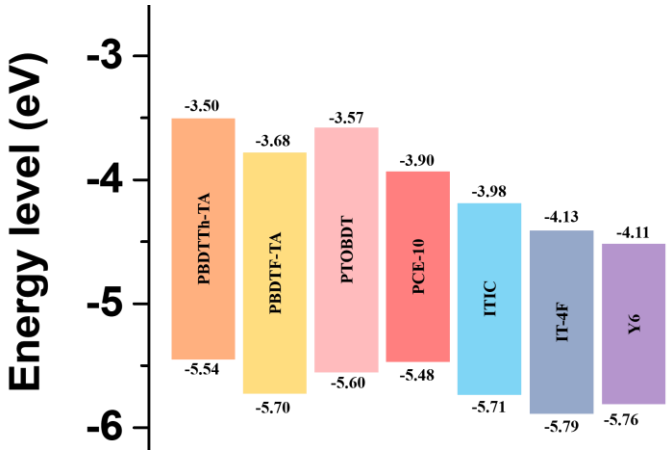

Figure 6 Relative frontier molecular energy level alignment of polymer donor and NFAs, discussed in this work.

1.4.2 **Donor material properties for a matching D:A combination**

1.4.2.1 High dielectric constant

The active layer materials with large dielectric constants in the range of silicon (~12) or perovskites (>20) can reduce the exciton binding energy (E_b; defined later), to enable highly efficient exciton dissociation.[14,66–68] The largely reduced exciton binding energy would require very small energy level offsets (ΔHOMO and ΔLUMO) for exciton dissociation, which could greatly reduce the energy loss and thus achieve a higher V_{OC}. In the ideal case a single component-organic solar cells device, where the polymer in the active layer has both donor and acceptor components, could greatly simplify the device fabrication process and achieve high morphological stability.[40] Jiang et al.[69], used this concept to achieve a record PCE of 8.40% in SC-OSC using a double-cable conjugated polymer.

Rule of mixtures for blend dielectric constant:

Rule of mixture is a simple model to predict the properties of a composite by calculating the weighted mean of the properties of the component materials. This rule can be applied here to

calculate blend dielectric constant (ε_{blend}) from the dielectric constants of component materials according to the following relation[41]:

$$\left(\frac{f}{\varepsilon_D}+\frac{1-f}{\varepsilon_A}\right)^{-1} \leq \varepsilon_{blend} \leq f\varepsilon_D + (1-F)\varepsilon_A \qquad 1.12$$

At the same time, the processes used for optimizing the active layer morphology also affect the material mixing, crystallinity, domain size, etc. These changes might reflect as the change in the relative permittivity.

1.4.2.2 Low exciton binding energy

After the absorption of a photon, the conjugated polymer generates a singlet excited state in which the electron and hole are bound by a strong Coulomb attraction: a singlet exciton. The Coulomb interaction is reflected as high binding energy for the exciton (E_b), which is greater than the thermal energy k_BT (~26 meV). For an efficient device performance, the photogenerated exciton should diffuse to the donor/acceptor interface (within the exciton diffusion length of ~20 nm)[14] so that exciton dissociation can occur. The dissociation of exciton would be easier if the E_b is lower.

1.4.2.3 High SCLC mobility

For efficient charge extraction capability in OSC devices (and reducing recombination and FF loss), high mobilities of both holes and electrons are crucial. As per a review of high-performance systems, blend carrier mobilities more than 10^{-4} cm^2 V^{-1} s^{-1} can achieve a reasonable FF of >70%. To achieve such moderate to high mobilities in the device, the polymer donor is preferred to have a planar backbone with moderate aggregation capability, predominantly face-on orientation, and covalent and noncovalent backbone rigidification induced by strategies such as fluorination[70], and/or side-chain modification[52,71]. Therefore, while modifying the properties of active layer material for increasing the dielectric constant and thus decreasing the singlet exciton binding energy E_b (and the charge transfer binding energy E_b^{CT} which is discussed in subsequent sections), the neat film SCLC mobility values

should be maintained (in the order of 10^{-4} cm^2 V^{-1} s^{-1}). The neat film SCLC mobilities of the donor and acceptors discussed in this thesis are listed in **Table 2**. All these materials have reasonable SCLC mobilities and therefore, the charge transport limitation in the blends can be expected to be low (although, unfavorable, too-mixed blend morphology in BHJ active layer can limit either or both electron and hole mobilities).

Table 2 Neat film SCLC mobilities of donor and acceptor materials.

Donor	**μ_{hole} [$\times 10^{-4}$ cm^2 V^{-1} s^{-1}]**
PTOBDT	3.64 ± 1.03
PBDTTh-TA	2.00 ± 0.94
PBDTThF-TA	0.90 ± 0.07
PCE-10	5.86 ± 0.64
P3HT	2.12 ± 0.27
Acceptor	**$\mu_{electron}$ [$\times 10^{-4}$ cm^2 V^{-1} s^{-1}]**
ITIC	1.60[a]
IT-4F	5.75[b]
Y6	6.2[b]
[a] taken from [72]; [b] and [c] taken from [73]	

1.5 Exciton binding energy and dielectric properties of polymer donors

In organic semiconductors, the absorption of photon means an excitation from the ground state (S_0) to the first excited singlet state (S_1) creating a singlet exciton with some specific binding energy (E_b) of 0.5-1.0 eV.[74]

Exciton binding energy is defined as the difference between the transport gap and the optical band gap:

$$E_b = E_g^t - E_g^{opt} \qquad 1.13$$

In the above equation, the optical band gap E_g^{opt} is the energy of the optically allowed first singlet state (S_1). The transport gap, E_g^t is generally defined as the difference between the ionization potential (IP) and electron affinity (EA) and is related to the delocalized states. E_g^{opt} can be determined experimentally from the absorption edge or at the intersection of absorption and emission spectrum.[28,75] The IP and EA can be measured by ultraviolet photoelectron spectroscopy (UPS) and inverse photoemission spectroscopy (IPES), respectively. Alternatively, the IP and EA values are usually measured by the more accessible cyclic voltammetry. However, for IPES, an ultrahigh vacuum (10^{-9} Torr) is needed which limits its widespread application. The electrochemical cyclic voltammetry (CV) directly injects charges into the LUMO and HOMO levels of solid-state films, providing an approximate measure of the transport gap energy. Although a simple and easily accessible method, CV values, so obtained, are consistently smaller than those obtained by photoemission and are also dependent on the experimental setup which means a large variation in HOMO/LUMO values can be found in the literature for the same material.[28,76,77]. At the same time, several polymer materials do not show a reduction potential in CV and E_g^t can not be accessed in such cases.

Recently, a simple and reliable method to obtain optical and transport gap energies for polymer donors, in a diode structure has been reported by Li et al.[76] which measures the E_b directly. This simple method is based on previous reports[78–82] where E_b is determined by measuring the photoconductivity quantum efficiency (or EQE/IQE) as a function of the photon excitation energy (or wavelength), measured in a polymer photodiode with a sandwich configuration of a semitransparent indium-tin-oxide (ITO) bottom electrode, a thin polymer layer (~100 nm), and an aluminum (Al) top electrode.[78]. This method was used to calculate the E_b values for six neat polymer donor materials which will be discussed in the next chapter.

Singlet vs charge transfer exciton binding energy: The singlet exciton formed upon absorption of light can dissociate either by a large applied electric field or at the interface with

another material with suitable energy offset, i.e., the donor-acceptor (D:A) interface.[14,74] For clarity, two types of exciton binding energies relevant to OSCs need to be differentiated.

The **(singlet) exciton binding energy**, E_b^{exc} (or simply E_b, hereafter) can be defined as the potential energy difference between the neutral singlet exciton and the two fully dissociated, structurally relaxed charge carriers in the same material. It can be measured using equation 1.14. In contrast, **charge-transfer-state binding energy**, E_b^{CT} represents the potential energy difference between the thermally relaxed, nearest neighbor charge-transfer state at the donor/acceptor interface and the two fully dissociated, structurally relaxed charge carriers in the donor and acceptor materials. The two types of binding energies can be visualized in **Figure 7** (adapted from Muntwiler et al.[74] and Tracey M. Clarke and James R. Durrant[14]).

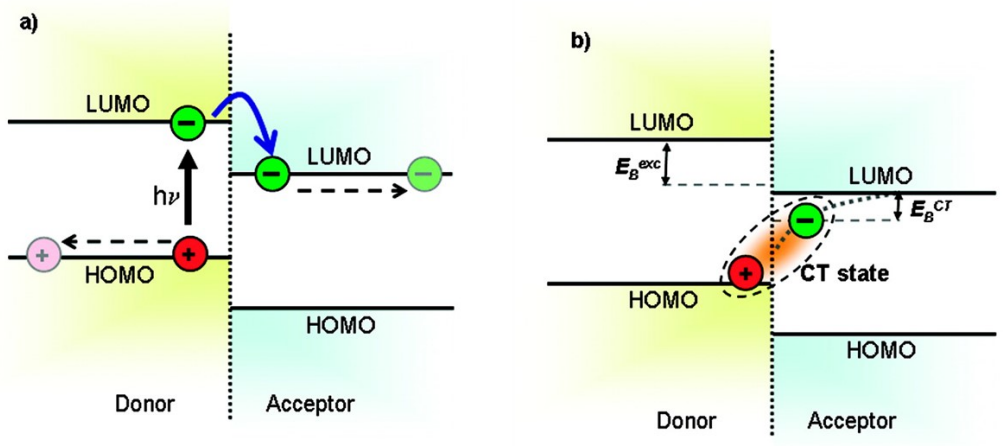

Figure 7 a) Energy level diagram of a donor/acceptor interface showing photoexcitation of an electron into the donor LUMO and electron transfer into the acceptor LUMO and migration of the separated charges away from the interface. (b) Visualization of typical binding energies for the exciton and CT states, E_B^{exc} and E_B^{CT}, respectively). Adapted from Muntwiler et al.[74] and Tracey M. Clarke and James R. Durrant.[14]

1.5.1 **Influence of dielectric constant (ε_r) on E_b**

Van der Horst et al.[83] did a theoretical calculation to show that the E_b in poly(p-phenylene vinylene) is of the form:

$$E_b(\varepsilon_r) = \frac{c}{\varepsilon_r^2} \qquad 1.14$$

where c is a constant and ε_r is the dielectric constant. In several other reports,[14,84,85] the exciton binding energy and the dielectric constant of the material follows the following relation:

$$E_b = \frac{e^2}{4\pi\varepsilon_0\varepsilon_r r} \qquad 1.15$$

where e is the elementary charge, ε_0 is the permittivity of vacuum, and r is the electron and hole separation distance.

From both the relations, it is obvious that increasing the dielectric constant should be the main approach towards decreasing E_b. Several methods have been proposed to increase the dielectric constant of the donor and acceptor materials: modifying side chains,[40] fluorination, etc.[86–88] For example, Xu et al.[86] showed that the fluorination can effectively increase the dielectric constant of naphthalene diimide (NDI)-based polymer acceptor by ~14% (from ~3.7 to 4.2).

1.5.2 **Influence of E_b and ε_r on OSC device performance**

A high dielectric constant (1) reduces the exciton binding energy; (2) reduces the Coulomb attraction within the CT exciton; (3) reduces geminate recombination back to the CT state; (3) reduces bimolecular and trap-assisted recombination; and (4) reduces space-charge effects.[14,74,89–91] An OSC based on high dielectric constant material, thus has the potential to reach the PCEs similar to that in inorganic solar cell materials.[90] Ibrahim et al.[89] put out a theory that if the dielectric constant of the active layer material can be increased significantly (to around 8 or higher), it is then possible that the mobility of the active material need not be

improved (from the current average values in the order of 10^{-4} cm^2 V^{-1} s^{-1}) in order to achieve the maximum efficiency. Moreover, the maximum achievable V_{OC}, while talking into account the CT exciton binding energy, can be expressed as[85]:

$$V_{OC}^{max} = IP_D - EA_A - \frac{e^2}{4\pi\varepsilon_0\varepsilon_r r_{DA}} \qquad 1.16$$

where ε_0 is the vacuum permittivity, ε_r is the relative dielectric constant of the bulk organic material, and r_{DA} is the initial separation in the charge transfer state.

Veldman et al.[25] found that the V_{OC} of an organic solar also depends on the dielectric constant of the blend: the charge transfer energy is reduced (charge transfer state shifts to a lower value) with an increase in dielectric constant, effectively reducing the V_{OC} of the device. On the other hand, Collins et al.[24], showed that the dielectric constant of several materials had an inverse relationship to the voltage losses measured. Thus, an increase in V_{OC} was attributed to reduced charge-carrier recombination losses. However, they put a condition that the energetic disorder should not be increased to increase the dielectric constant.

Duan et al.[87] showed that optimally annealed devices showed the largest dielectric constant (13.11 vs 6.35 for 80°C-annealed vs fresh devices, respectively) inducing more efficient charge separation. They proposed that thermal annealing can tune the dielectric property and reduce the energetic disorder for PffBT4T-2OD donor-based devices.

Zhang et al.[92] used a fluorinated PBDBT-2F donor and fluorinated IT-4F acceptor which enhanced the dielectric constant in the blend film (as compared to that with a non-fluorinated ITIC acceptor). Consequently, PBDBT-2F:IT-4F-based device obtained higher FF, while higher J_{SC} and lower V_{OC} can be attributed to the lower-lying $LUMO_A$ and lower bandgap of IT-4F. The enhancement in FF was studied in detail, and a lower geminate and non-geminate (bi-molecular) recombination was found, attributing it to enhanced dielectric constant. However, the impacts of fluorination on the dielectric properties and the key processes of charge dissociation and recombination need investigation since they are poorly understood and not often discussed in depth.[86] Another reason is to explore this topic is the observation that

increasing the dielectric constant (dipole moment) of a polymer would not always result in better solar cell performance; for example, adding polar groups in order to increase the dipole moment might also lead to unwanted trapping centers within the molecule, thus increasing recombination.[93]

1.6 Aim and scope of this thesis

The objective of this thesis is to understand (a) the effect of molecular structure on dielectric constant and the relation of dielectric constant with the exciton binding energy, of neat polymer donors, and (b) the effect of processing conditions and polymer donor dielectric constant on the dielectric constant of donor:NFA blend in the OSC devices.

In Chapter 2, the influence of the dielectric constant on the singlet exciton binding energy (E_b) will be studied. The effect of increasing dipole moment (for example by adding fluorine atom on the backbone) will also be discussed.

In Chapter 3, the influence of processing conditions (thermal annealing and DIO additive addition) and dielectric constant of donor (and NFA used as the acceptor in the blend) materials on the dielectric constant of the blends will be explored in relation to the observed device performance.

Finally, a summary of the observations for a better understanding of the influence of dielectric constant on OSC device performance will be provided.

Chapter 2

Influence of dielectric constant on exciton binding energy of donor polymers

2.1 Introduction

A bound pair of an electron and a hole is produced upon photo-absorption which then dissociates at the donor:acceptor interface in OSC devices. In an efficient OSC device, the geminate electron and hole should avoid mutual recombination, so that they can become free charge carriers and contribute to the generated photocurrent. It is generally expected that increasing the dielectric constant (ε_r) of the polymer donor effectively lowers the exciton binding energy (E_b) (according to equations 1.14 and 1.15 and thus, helps reduce geminate recombination (recombination of electron-hole from the same material before separation) losses in the organic solar cells.

In this chapter, the exciton binding energies, and dielectric constants of six polymer donors are measured and the relationship between the two parameters is studied. At the same time, the effect of molecular structure on these two properties is also discussed.

2.2 Experimental Section

2.2.1 Materials

The synthesis and characterization (NMR spectra, elemental analysis, GPC analysis, electrochemical analysis, etc.) of all intermediates and polymers were done by our group. P3HT and PTOBDT polymer were synthesized by Dr. Keqiang He, and PBDTTh-TA, PBDTTh-TC, and PBDTThF-TA were synthesized by Yi Yuan and the relevant manuscripts detailing synthesis will be published later in 2021. All the other active layer materials: PCE-10, ITIC, IT-4F, and Y6 were procured from 1-Material. The molecular weights are listed in **Table 3.**

Table 3 Molecular weights of the studies polymer donors.

Polymer	M_n **(kDa)**	M_w **(kDa)**	$Đ$
PBDTTh-TA	27.4	47.6	1.7
PBDTTh-TC	66.1	17.2	2.6
PBDTThF-TA*	-	-	-
PTOBDT	109.5	195.8	1.8
PCE-10	76.0	190.0	2.5
P3HT	56.6	33.1	1.7
*under acquisition and will be published along with synthesis related information by our group.			

2.2.2 **Fabrication and characterization of ITO/polymer/Al diodes**

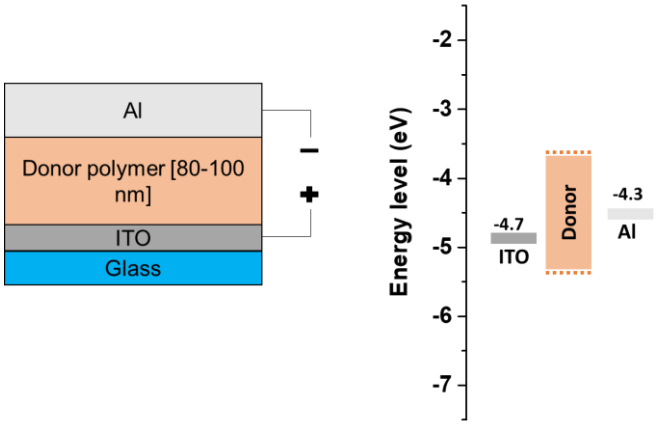

Figure 8 Device structure and energy levels in the device for EQE and impedance measurement.

The diodes for EQE and capacitance-frequency measurements were fabricated in a structure of ITO/active layer (~80-100 nm)/Al (100 nm) (**Figure 8**)). ITO glass substrates were ultrasonicated for 20 min sequentially in de-ionized water, acetone, and isopropanol,

respectively. Then the substrates were treated with plasma for 15 mins. The substrates were transferred to a nitrogen-filled glove box, where the polymer blend layer (~100 nm) was spin-coated onto ITO with the optimized RPMs. The solutions were stirred at 50 °C for 3 h before coating. After that, the active layers were thermal annealed at 100 °C for 10 min before being transferred into a vacuum chamber. Finally, at P ≈ 5.0 × 10^{-6} Pa, a layer of Al (100 nm) electrode was coated onto the substrate. The active area is 0.0574 cm^2. The EQE of the devices was measured using an ORIEL IQE200B system by Newport. Capacitance-frequency measurements were done on BioLogic VSP in the frequency range 100 Hz – 1 MHz, in dark. Thicknesses were measured using a profilometer (Alpha Step D500 from KLA), taking an average of four spots on each of the substrates to minimize the error from non-uniformity of the coated film (5-10%).

2.2.3 **DFT calculation of charge distribution and dipole moment**

Density functional theory (DFT) calculations were carried out by using Gaussian 09 with a hybrid B3LYP correlation functional and 6-31G (d) basis set to estimate the magnitude and direction of changes to the permanent dipole upon molecular structure changes.

2.3 Results

Diode structure ITO/polymer/Al was used to measure the EQE of the neat polymer device. The exciton binding energies estimated from the primary and secondary onset energy difference (according to the method reported by Li et al.[76]) of six polymer donors are listed in **Table 4**, while the EQE spectrum is shown in **Figure 9**. The EQE values are quite low for all the polymers since these polymers have higher hole mobilities than the electron mobilities, creating an imbalance in the charge transport. All the polymers show two distinct onsets and a plateau region in between: the first excitation energy is equal to the E_g^{opt} of the polymer. The plateau region corresponds to the first excitation state (S_1) and its vibrational levels.[76] The second onset is characterized by a large enhancement in the EQE which is independent of the absorption profile, confirmed earlier by Li et al.[76] This onset is attributed to the dissociated charges, thus giving access to the delocalized state (transport level, E_g^t).[79,80] The E_b values are then calculated from the difference between these two onsets.

P3HT has the highest exciton binding energy (0.70 eV, similar to the reference[76]) among these polymers. "Push-pull" polymers have larger dipole moment and thus generally lower E_b. The smallest E_b (0.41 eV) was obtained for PBDTTh-TA polymer donor, while the commercial polymer PCE-10 showed E_b of 0.685 eV.

Dielectric constants were calculated in the same EQE devices, in the frequency range 100 Hz-1 MHz and the values obtained at 10 kHz frequency, are listed in **Table 4**, while the frequency dependency is shown in **Figure 10**. An inverse relation between E_b and dielectric constant (as suggested by equations 1.14 and 1.15), does not seem to hold for this list of polymers and therefore a linear relationship (Coulomb's law) could not be found in the E_b vs 1/dielectric constant plot in **Figure 11** (neither in E_b vs 1/dielectric^2). One reason for this observation could be the different effective conjugation lengths for different polymer materials in thin solid films due to different packing behaviors. For example, Knupfer[94] found that the previously reported values for the exciton binding energies in many organic materials differed from the measured values by more than an order of magnitude, which he rationalized with a simple dependence of the exciton binding energy on the length of the molecular units. Since these polymers are relatively amorphous, synchrotron-based grazing angle wide-angle measurements (GIWAXS) can be used to obtain information about the packing behaviors of crystallites.[95–97]

Table 4 Exciton binding energy of neat polymer films calculated using the EQE method.

Polymer	**Exciton binding energy, Eb (eV)**	**Dielectric constant, ε**
PBDTTh-TA	0.415 ± 0.057	3.78 ± 0.06
PBDTTh-TC	0.430 ± 0.036	3.55 ± 0.21
PBDTThF-TA	0.672 ± 0.011	4.72 ± 0.43
PTOBDT	0.452 ± 0.060	4.21 ± 0.33
P3HT	0.702 ± 0.046	3.72 ± 0.17
PCE-10	0.685 ± 0.005	4.05 ± 0.11

*All the values presented in the table are the average and standard deviation of at least four diodes.

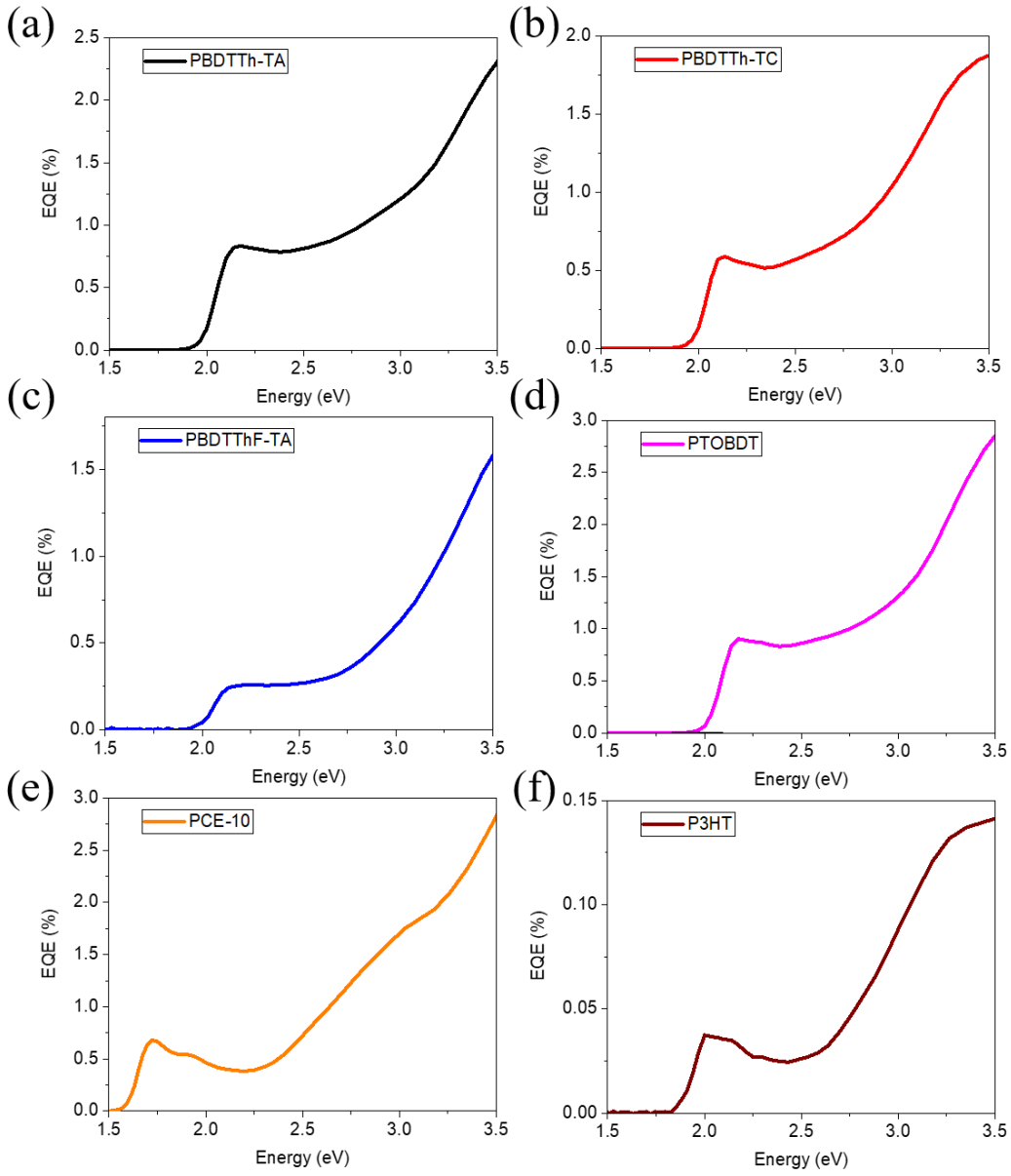

Figure 9 EQE spectra of neat polymer films showing primary and secondary onsets.

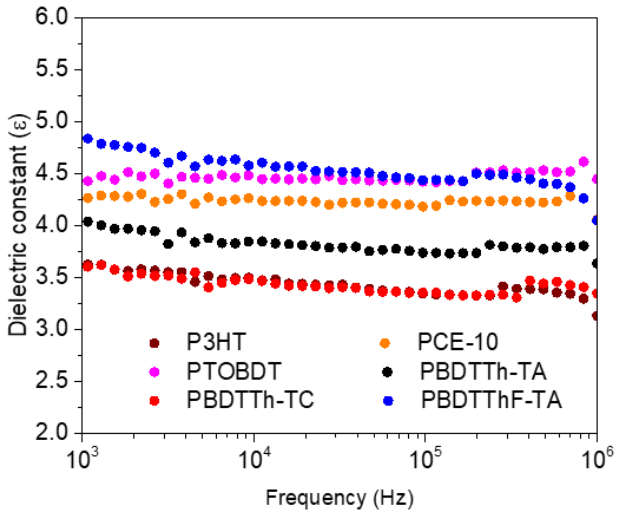

Figure 10 Dielectric constant of donor polymers.

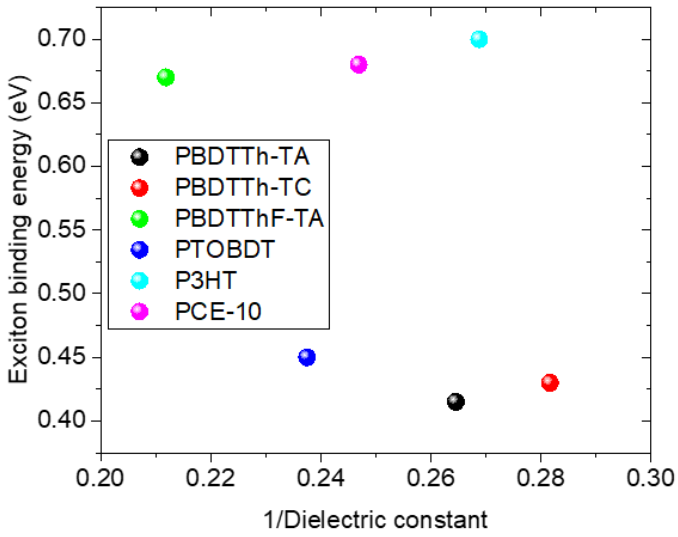

Figure 11 Exciton binding energies of the photovoltaic polymers determined by EQE versus the inverse of dielectric constant of the polymers measure at 10 kHz.

Dipole moment vs polarity of donor monomers:

Dipole moment (based on charge distribution/polarity in the ground state) was calculated using DFT via Gaussian 9. The dipole moment in Gaussian is defined with respect to the center of the positive charge. The dipole moment calculation can be an effective way to predict the dielectric constant variation in similar molecules along with the net dipole direction with respect to the backbone plane (as shown in **Figure 12**).

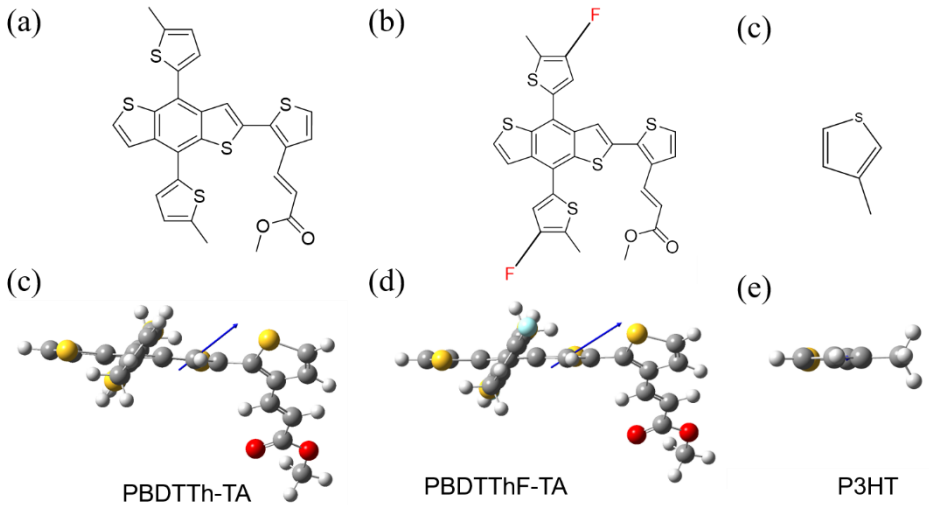

Figure 12 Simplified chemical structure for DFT calculation: (a) PBDTTh-TA, (b) PBDTThF-TA, and (c) P3HT. Net dipole moment calculated using DFT: (c) PBDTTh-TA, (d) PBDTThF-TA, and (e) P3HT. Blue arrow shows the direction of dipole moment. In P3HT the dipole moment vector is on plane of the thiophene ring.

In OSCs where the charge transport takes place in the vertical direction, the donor polymers should arrange preferentially in π-π stacking. In this case, the backbone of the polymer should align in-plane with the substrate. Therefore, if the net dipole moments (shown using arrows in **Figure 12**) point away from the plane of the backbone (preferable perpendicular to the substrate), the effective dielectric contribution will be higher for the vertical charge transport.

Table 5 Dipole moment and dielectric constant.

	ε_r [1]	**Net Dipole (Debye)**
PBDTTh-TA	3.78 ± 0.07	1.1550
PBDTThF-TA	4.72 ± 0.43	1.3031
P3HT	3.72 ± 0.17	0.3364

[1] Average and the standard deviation is taken from at least 4 devices

From the dipole moments and dielectric constant values in **Table 5,** fluorination can effectively increase the dielectric constant, and that the "push-pull" polymers, generally have a higher polar character and higher dielectric constant than homopolymers like P3HT. But while increasing dielectric constant, the SCLC mobility of fluorinated polymer (PBDTThF-TA) decreased slightly from 2.0×10^{-4} to 0.90×10^{-4} cm^{-2} V^{-1} s^{-1} (**Table 2**). This trade-off and its adverse impact (if any) will be analyzed in OSCs based on these two polymers (in Section 3.4).

2.4 Summary and conclusions

In summary, the measured E_b values of the polymers synthesized in our lab have lower exciton binding energy than those of commercial polymers (P3HT and PCE-10). Therefore, one can expect better performances from these polymers since the mobility values are also in the same order (~10^{-4} cm^2 V^{-1} s^{-1}).

Fluorinated polymer PBDTThF-TA has a higher dielectric constant than the non-fluorinated counterpart PBDTTh-TA, confirming the contributions from increased dipole moment due to F atom. However, contrary to the general assumption, the E_b did not decrease by increasing the dielectric constant. This observation is significant since simply increasing the polarity to increase the dielectric constant would not necessarily decrease the E_b. In addition, adding F in

the backbone decreased the hole mobility, therefore, the net effect of an increase in dielectric constant for this polymer might not prove beneficial.

It is important to emphasize that the dielectric constants calculated for these polymers represent the average of the dipole moments in the direction perpendicular to the substrate along the thickness direction (~100 nm). In reality, the exciton formation is an intramolecular process, and therefore the bulk dielectric constant might not correlate directly with the exciton binding energy.

The dipole moment of the monomer of PBDTTh-TA was lower than that of the fluorinated polymer PBDTThF-TA, which still does not establish an inverse relationship between dipole moment and E_b. A possible variable that needs to be taken into account is the dipole moment of the excited states. The dipole moment calculations in this chapter were done in the ground state, while the E_b calculation (EQE measurement) involves an excited state in the formation of exciton and subsequent separation into free electrons and holes. The excited-state dipole moments would more closely represent the polarization that the exciton experiences. When the difference between the ground and the excited state dipole moment increases enough, the excitons can even "pre-separate", thus lowering the effective Coulomb binding energy as suggested by Carsten et al.[93,98]

Furthermore, in order to increase the accuracy of dipole moment calculation, multiple repeat units of monomers should be simulated which can provide information regarding loss/increase in symmetry with multiple units, which can effectively influence the local dipole moments.

Chapter 3

Dielectric constant of blends in organic solar cells

3.1 Introduction

In a bulk heterojunction (BHJ) structure, the donor and acceptor materials are blended in a common solvent, which achieves a sufficiently mixed morphology to maximize the interfacial area, while maintaining percolation paths to the respective contacts, for the electrons and holes in the acceptor and donor domains, respectively. Therefore, the morphology optimization methods aim to achieve high average domain purity and highly ordered packing of both donor and acceptor to minimize charge recombination in the OSCs.[99] Thermal annealing and processing solvent additives[100] are well-known blend morphology optimization methods. The nanoscale phase separation (or miscibility) in the blend also depends on the characteristics of the constituent materials along with the specific processing conditions. These variations in the processing conditions and material properties reflect in domain size, domain purity, domain crystallinity, and intermixing of donor and acceptor in blend active layer; these variations impact the overall performance directly. Although BHJ solar performs better than bilayer (with donor/acceptor material coated separately), the prediction and characterization of several important parameters become complicated because the blend would have very different properties than the individual components.

In 1.5.2, it was argued that the dielectric constant of the blend is of paramount importance, since it determines the extent of recombination in the device, thus affecting both FF and V_{OC} of the device. Also, the dielectric constant of the blend depends on both processing conditions and the properties of the donor/acceptor as reported elsewhere[48,86,92,98,101–103].

In this part of the thesis, the effects of processing conditions and the dielectric constants of the donors (in combination with NFA acceptors) on the dielectric constants of the blends have been studied. The effect of the dielectric constant will be mainly visible on the FF and V_{OC} of the devices (as discussed in 1.5). Therefore, in order to differentiate the effect of dielectric constant from other device parameters which also affect V_{OC} and FF (such as active

layer/contact interfaces, energy level alignments, and mobilities, etc.), have also been studied to provide a complete picture of the device performance.

This chapter is divided into two parts: Part I concerns the effects of annealing and additive addition, while in Part II, the effects of material design (fluorination) are investigated.

3.2 Experimental section

3.2.1 **Fabrication and characterization of organic solar cells**

The following device structure (**Figure 13**) was used for organic solar cell devices and impedance measurements**.**

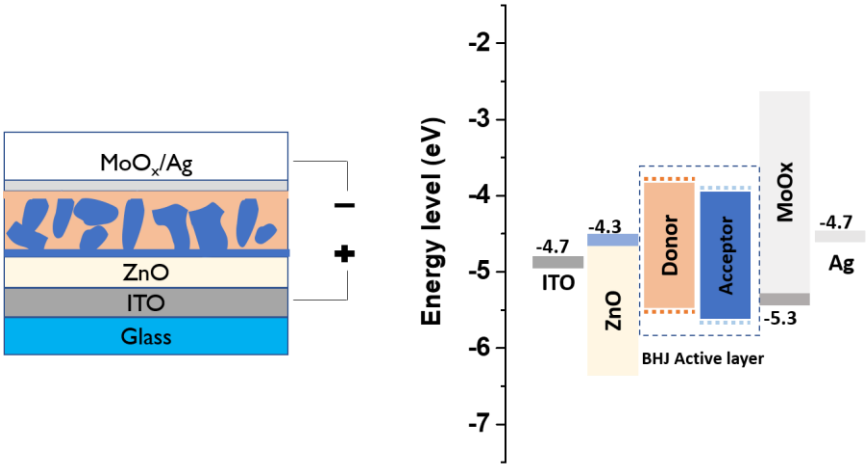

Figure 13 Device structure used in OSC devices.

The OSC devices were fabricated in an inverted structure of ITO/ZnO (40 nm)/active layer/MoO_x (10 nm)/Ag (100 nm). ITO glass substrates were ultrasonicated for 20 min sequentially in de-ionized water, acetone, and isopropanol, respectively. The ZnO precursor was prepared by mixing Zinc acetate (197 mg), Ethanolamine (54 µl), and 2-methoxyethanol (2 ml). After stirring vigorously at RT overnight, the solution was filtered through a 0.45 µm PTFE syringe filter. Then the substrates were treated with plasma for 15 mins. A thin layer of

ZnO was deposited through the spin coating at 3500 rpm for 60 s and annealed at 200 ℃ for 1 h in the air. The substrates were transferred to a nitrogen-filled glove box, where the D/A blend layer (~ 100 nm) was spin-coated onto the ZnO layer with the optimized RPMs. The D:A blends were dissolved in CF (and CF + 1% v/v DIO) and the weight ratio is 1:1.2 with a total concentration of 16 mg/mL in the glove box for PTOBDT:Y6 blends. For the blends based on donors PBDTTh-TA and PBDTThF-TA and NFAs ITIC and IT-4F, o-DCB was used as the solvent in the weight ratio of 1:1 (D:A) with a total concentration of 40 mg mL^{-1}. The solutions were stirred at 50 °C for 3 h for CF-based blends and at 80 °C overnight for o-DCB based solutions. After spin coating, the active layers were thermal annealed at specific temperatures for 10 min before transferring into a vacuum chamber. Finally, at P ≈ 5.0 × 10^{-6} Pa inside a thermal evaporator (Model: Covap, Angstrom Engineering), a thin layer of MoO_x (10 nm) and a layer of Ag (100 nm) were both deposited onto the active layer. The active area is 0.0574 cm^2. The current density-voltage (J-V) characteristics of the devices were measured on an Agilent B2912A Semiconductor Analyzer with a Science Tech SLB300-A Solar Simulator. A 450 W xenon lamp and an air mass (AM) 1.5G filter were used with the light source. EQE was measured using ORIEL IQE200B from Newport.

3.2.2 **PL quenching**

Photoluminescence spectra were recorded on Horiba PTI QuantaMasterTM 8000 Series Fluorimeter. Neat and blends films were prepared on ITO/ZnO substrates. PL quenching efficiency is defined as[104]:

$$PLQE = 1 - \frac{PL_{blend}}{PL_{neat}} \qquad 3.1$$

where PL_{blend} and PL_{neat} are the integral PL counts of blends and neat films, respectively.

3.2.3 **SCLC mobility**

The SCLC hole mobility is measured in hole-only devices, employing a device architecture of ITO/PEDOT:PSS (~30 nm)/active layer)/MoO_x (10 nm)/Ag (100 nm), while the SCLC

electron mobility is measured using a device architecture ITO/ZnO (40 nm)/active layer/LiF (1 nm)/Al (100 nm). J-V curve obtained in dark is used to fit the following equation 1.5.

3.2.4 **AFM**

AFM images of the blend films coated on ITO/ZnO substrates were recorded on a Dimension 3100 scanning probe microscope.

3.2.5 **Surface tension characterization**

Contact angles were measured using a high-resolution Canon DSLR camera and the edge detection/angle measurements were done using an image analysis software ImageJ®[105]. Since the angles were measured manually, only one digit after decimal was taken to account for the limited precision. Neat films were coated on ITO/ZnO substrates and annealed at the same temperature as the device. The surface tension values were calculated using Wu's model discussed in 1.3.9.

3.2.6 **Impedance analysis**

Capacitance-voltage curves were obtained at a frequency of 10 kHz with sweeping voltage from -2 to +2V at an AC perturbation of 10 mV on the BioLogic VSP potentiostat. Capacitance frequency curves were obtained for the frequency range 100 Hz-1 MHz, on the same system. Both measurements were done in dark.

3.3 Results and discussion: Part I- Effect of processing parameters on blend dielectric constant

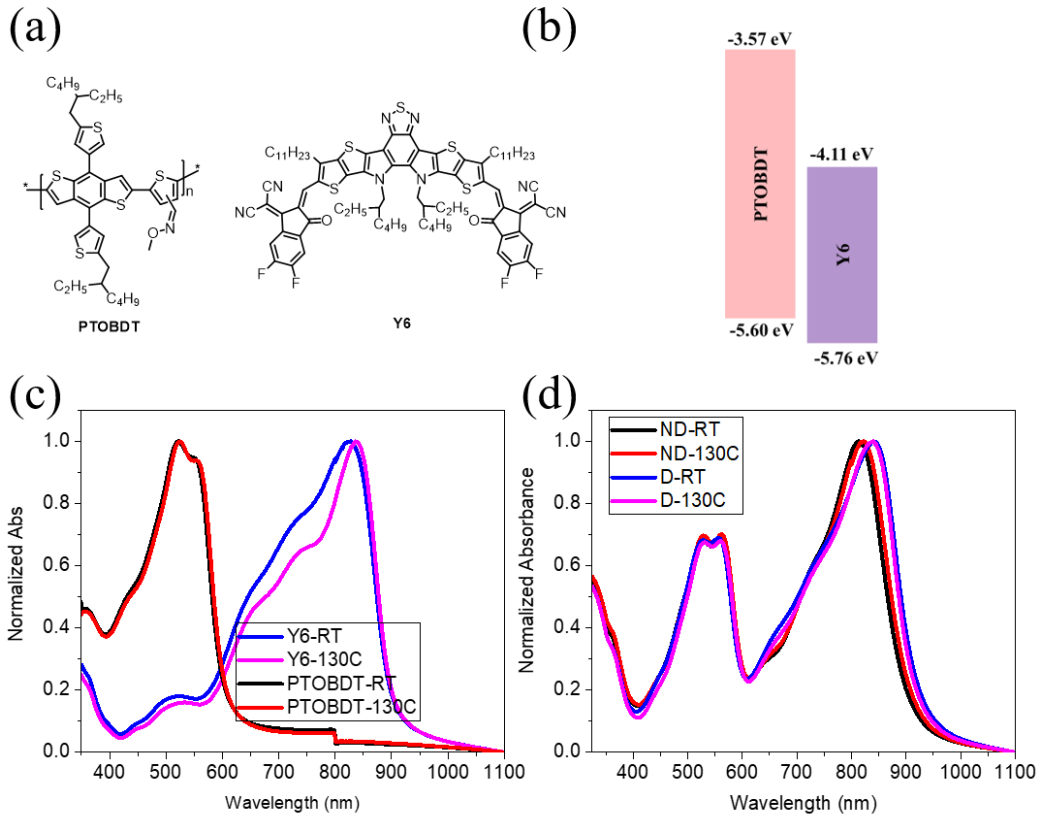

Figure 14 (a) Chemical structures of PTOBDT and Y6; (b) frontier energy levels of PTOBDT and Y6 thin films; UV-vis spectra of (c) PTOBDT and Y6 films (as cast and 130 °C annealed) and (d) blend films: with/without 1% v/v DIO additive of as cast (RT) and 130 °C-annealed films. **Key**: PTOBDT:Y6 blends with different processing conditions: **ND-RT**: without DIO and as cast; **ND-130C**: without DIO and annealed at 130 °C; **D-RT**: with DIO and as cast; **D-130C**: with DIO and annealed at 130 °C.

The chemical structures, energy level alignment, and absorption spectrum of neat and blend films, of the donor polymer (PTOBDT) and non-fullerene acceptor (Y6) are shown in **Figure 14**. A complementary absorption and sufficient ΔHOMO and ΔLUMO offsets can be seen in this particular donor:acceptor combination, which would lead to high performance in the BHJ solar cells.

3.3.1 **Photovoltaic performance**

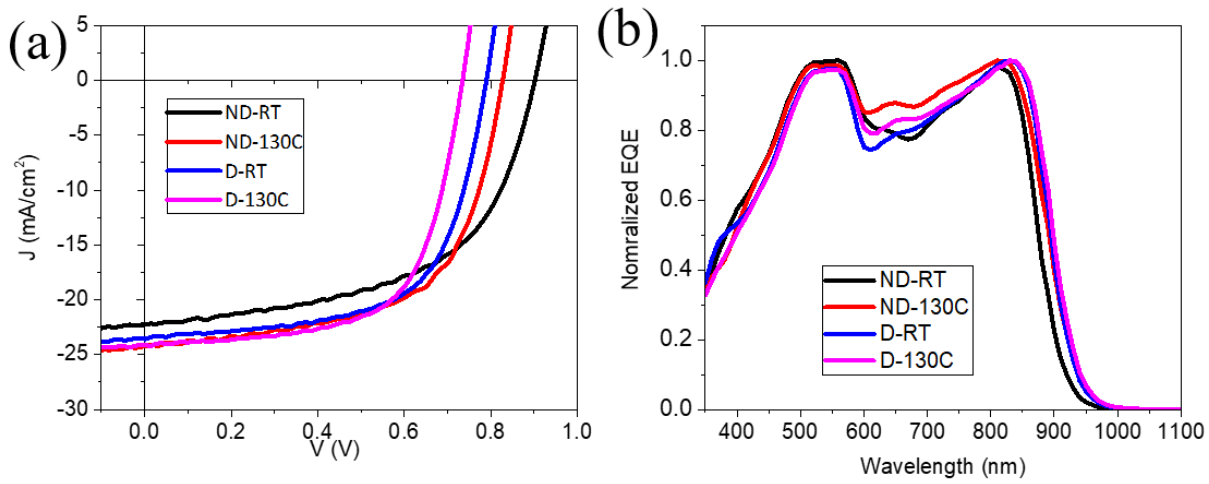

Figure 15 (a) J-V curves and (b) Normalized EQE for PTOBDT:Y6 blends with/without annealing and DIO additive addition.

OSCs with device structures of ITO/ZnO/PTOBDT:Y6/MoO_x/Ag were fabricated. The active layers were processed at RT and 130°C for studying the effects of annealing temperature on the blend dielectric constant and thus on the photovoltaic performance of the solar cells. Furthermore, to study the effects of DIO, 1% v/v DIO was added to the CF solvent with the same annealing conditions. The thickness of the active layers was optimized and found to be 100 ± 5 nm for all the solar cells. The corresponding photovoltaic parameters are shown in **Table 6**.

Table 6 Photovoltaic performance data of best PTOBDT:Y6 devices (average values are in parentheses).

	Jsc [mA cm^{-2}]	**Voc [V]**	**FF**	**PCE [%]**	**J_{sat}**	**P_{dis}**	**P_{coll}**
Without additive							
ND-RT	22.15 (21.36)	0.91 (0.905)	0.56 (0.565)	11.19 (10.91)	24.87	89.14	66.59
ND-130C	24.72 (23.81)	0.84 (0.83)	0.62 (0.61)	12.84 (12.19)	26.45	91.68	71.08
With DIO additive							
D-RT	23.88 (22.16)	0.80 (0.80)	0.65 (0.65)	12.28 (11.44)	25.14	93.68	74.26
D-130C	24.62 (24.34)	0.74 (0.74)	0.66 (0.65)	12.02 (11.73)	25.85	93.27	76.25

Key: PTOBDT:Y6 blends with different processing conditions: **ND-RT**: without DIO and as cast; **ND-130C**: without DIO and annealed at 130 °C; **D-RT**: with DIO and as cast; **D-130C**: with DIO and annealed at 130 °C.

The PTOBDT:Y6 devices with no DIO additive (ND), annealed at 130°C (ND-130C) demonstrated the highest PCE of 12.84%, while those without annealing showed a PCE of 11.19%. FF improved upon annealing while V_{OC} decreased. Both DIO additive based devices, without annealing (D-RT) and with annealing at 130°C (D-130C), showed improved FF compared to those without the additive. However, a significant drop was observed in the $V_{OC,}$ with PCEs of 12.28% for D-RT and 12.02% for D-130C.

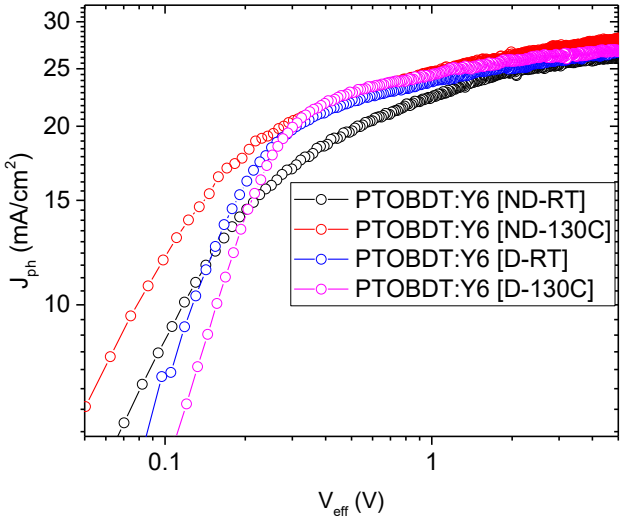

Figure 16 Photocurrent vs Effective voltage plot for PTOBDT:Y6 devices.

Exciton dissociation, collection, and recombination: The trend of photocurrent density J_{ph} ($J_{ph} = J_L - J_D$, where J_L is the current density under illumination and J_D is the current density in dark) versus effective voltage ($V_{eff} = V\text{-}V_0$), gives insights into the charge generation and exciton dissociation characteristics of the device. Here V_0 is called the compensation voltage or the voltage at which $J_{ph} = 0$ and V is the applied voltage.[55,106] J_{ph} reaches a saturation value (J_{sat}) with increasing V_{eff}, which means that all the photogenerated excitons are dissociated into free carriers and collected by the electrodes with the assistance of large reverse bias. Thus, the exciton dissociation probability, defined as $P_{diss} = J_{SC}/J_{sat}$, reflects the efficiency of exciton dissociation, charge transport, and charge collection.[55] Devices with DIO additive (both D-RT and D-130C) showed slightly better exciton dissociation probabilities (**Table 6**), while the

charge collection probability (P_{coll}) was slightly higher for the annealed device (D-130C) consistent with the FF values. In devices without the DIO additive, improvement in both P_{diss} and P_{coll} was seen upon annealing, supporting the OSC performance with increased FF and J_{SC} for the annealed device (ND-130C).

In the blend absorption spectrum (shown in **Figure 14**d) and EQE spectrum (shown in **Figure 15**b) with DIO additive, a redshift of absorption (EQE) edge was seen (ND-130C: 910 nm vs D-130C: 923 nm), suggesting an increase in crystallinity/packing of the acceptor domains (**Figure 14d**), since no redshift in donor peak positions were observed. This narrowing of effective bandgap can be one of the contributors to the V_{OC} decrease in DIO additive based devices. Although this variation was ca. 0.03 eV, which cannot fully account for V_{OC} difference (ΔV_{OC}) of 0.1 V with respect to the devices without DIO additive.

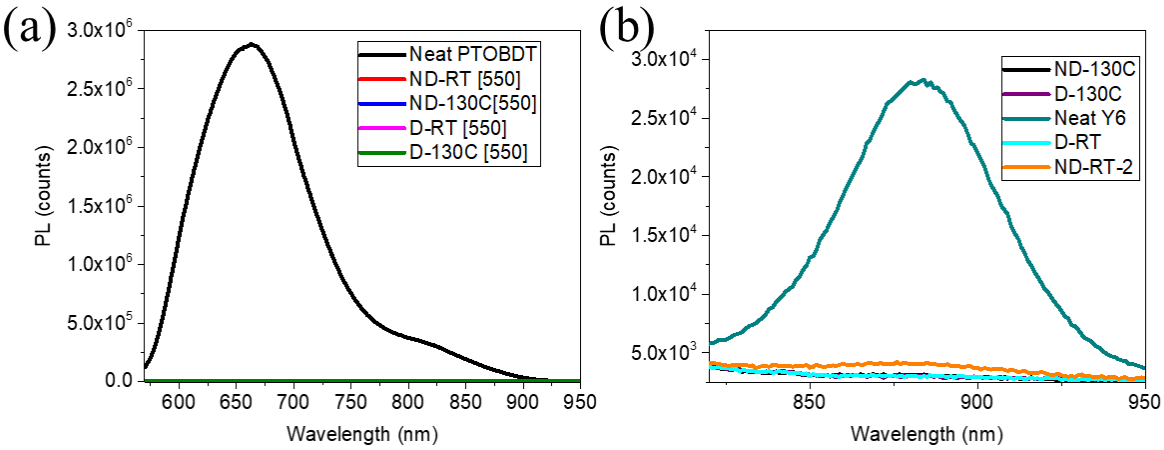

Figure 17 PL quenching of PTOBDT:Y6 blend. Donor and acceptor were selectively excited at 550 nm and 800 nm, respectively.

Table 7 Effect of DIO addition and annealing temperature on PL quenching in PTOBDT:Y6 blends.

	$PLQE_D$ [%]	**$PLQE_A$ [%]**
Without additive		
ND-RT	>99.9%	97%
ND-130C	>99.9%	>99.9%
With DIO additive		
D-RT	>99.9%	>99.9%
D-130C	>99.9%	>99.9%

Key: PTOBDT:Y6 blends with different processing conditions: **ND-RT**: without DIO and as cast; **ND-130C**: without DIO and annealed at 130 °C; **D-RT**: with DIO and as cast; **D-130C**: with DIO and annealed at 130 °C.

Photoinduced charge transfer efficiency (from donor to acceptor or vice versa) can also be probed via photoluminescence (PL) quenching and decay measurements of the blend films relative to the neat films.[29,30] The quenching efficiency gives information about the nanoscale morphology and miscibility of donor and acceptor domains within the blend layer, which is often not directly accessible via surface characterization techniques like AFM[104]. All the four blends were able to quench the donor PL ($PLQE_D$ >99.9%), suggesting an effective diffusion of excitons and transfer of electrons from donor to acceptor, while the efficiency of hole transfer from acceptor to the donor ($PLQE_A$) was slightly lower in the ND-RT device, partly accounting for the slight decrease in J_{SC}. The other three blends (ND-130C, D-RT, and D-130C) had a high $PLQE_A$ of >99.9% (PL spectrum and PLQE values are presented in **Figure 17** and **Table 7** respectively).

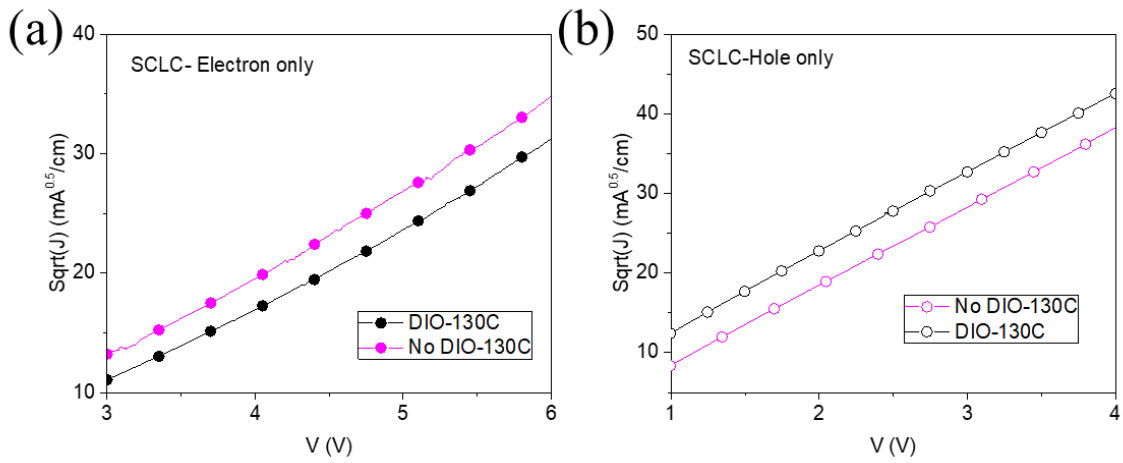

Figure 18 SCLC blend (a) electron and (b) hole mobilities of PTOBDT:Y6 devices with/without annealing and DIO additive addition.

Table 8 SCLC mobilities of PTOBDT:Y6 blends.

	μ_{hole} [$\times 10^{-4}$ cm^2 V^{-1} s^{-1}]	$\mu_{electron}$ [$\times 10^{-4}$ cm^2 V^{-1} s^{-1}]
	Without additive	
ND-130C	2.35 ± 0.59	2.45 ± 0.61
	With DIO additive	
D-130C	4.97 ± 0.75	1.85 ± 0.54

Key: PTOBDT:Y6 blends with different processing conditions: **ND-130C**: without DIO and annealed at 130 °C; **D-130C**: with DIO and annealed at 130 °C.

Charge transport was characterized to account for the difference in FF of the annealed devices with DIO (D-130C) and without DIO (ND-130C) additive, which has the best FFs among the two groups (**Figure 18** and **Table 8**). The device without DIO additive showed SCLC μ_{hole} and $\mu_{electron}$ of $2.35 \pm 0.59 \times 10^{-4}$ and $2.45 \pm 0.61 \times 10^{-4}$ $cm^2 V^{-1} s^{-1}$, respectively. In the devices with DIO, slightly higher μ_{hole} ($4.97 \pm 0.75 \times 10^{-4}$ $cm^2 V^{-1} s^{-1}$), and a lower $\mu_{electron}$ ($1.85 \pm 0.75 \times 10^{-4}$ $cm^2 V^{-1} s^{-1}$) were observed. In both devices, sufficiently high SCLC mobilities and low $\mu_{hole}/\mu_{electron}$ ratio were observed. An increase in blend hole mobility in D-130C might suggest morphological and crystal packing changes in polymer donor but could not directly account for the significant increase in FF of the D-130C device since the electron mobility did not improve in the same proportion.

3.3.2 **Dielectric constant and built-in potential**

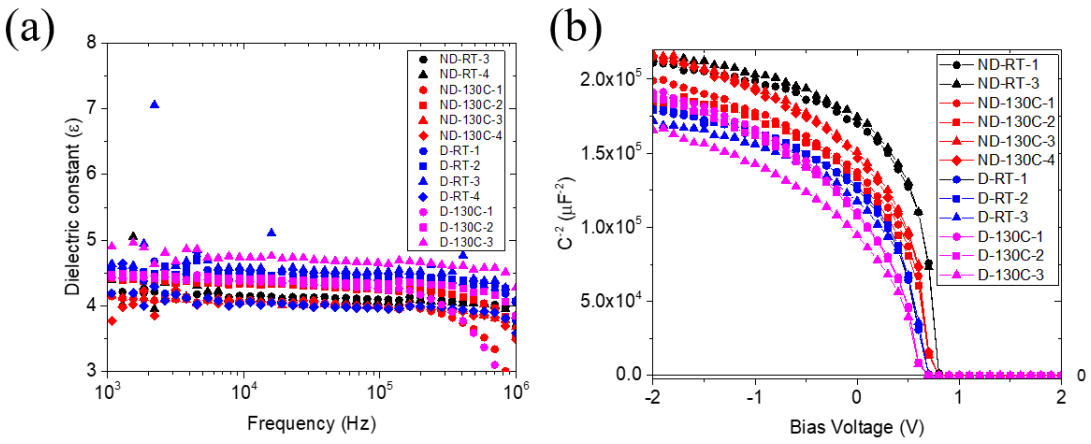

Figure 19 (a) Dielectric constant and (b) Mott-Schottky plot for blends with/without annealing and DIO additive.

Table 9 V_{bi} and dielectric constant of PTOBDT:Y6 blends.

	V_{bi} [V]	ε_r
Without additive		
ND-RT	0.802 ± 0.002	4.145 ± 0.005
ND-130C	0.727 ± 0.005	4.128 ± 0.117
With DIO additive		
D-RT	0.685 ± 0.005	4.440 ± 0.262
D-130C	0.617 ± 0.005	4.510 ± 0.164

Key: PTOBDT:Y6 blends with different processing conditions: **ND-RT**: without DIO and as cast; **ND-130C**: without DIO and annealed at 130 °C; **D -RT**: with DIO and as cast; **D-130C**: with DIO and annealed at 130 °C.

In the previous section, it was shown that the lowest J_{SC} value for non-annealed, without additive (ND-RT) could be accounted for by the J_{sat} values (since J_{sat} (at V_{eff} = 3V) is the maximum current that the device could produce). However, the V_{OC} and FF values (which vary considerably) need more analysis since the Voc values are generally assumed to be linearly related to the difference between the LUMO of the acceptor and HOMO of the donor. In this case, with the same D:A blends, the large differences in V_{OC} values (ΔV_{OC}) from 0.91 V in ND-RT to 0.74 V in D-130C, would suggest interfacial or blend morphology changes (as discussed in the introduction chapter). As already discussed, the effect of bandgap narrowing (absorption and EQE redshift) could not account for the total $\Delta V_{OC.}$ Also, the SCLC mobilities could not account for the increased FF in the DIO based devices, since the mobility ratio increased because of an increase in the hole mobility.

The dielectric constant of blends could explain both FF and V_{OC} change, as discussed in section 1.5. Therefore, the dielectric constants of all four devices were calculated. The values obtained at 10 kHz frequency are listed in **Table 9** and the frequency dependence of the dielectric

constant is plotted in **Figure 19**a. It can be observed that the dielectric constant values (average values from 3-4 devices) of the blends are similar in all the devices. Noticeably, these values are close to the weighted average ($f\varepsilon_D + (1-f)\varepsilon_A$ = 4.03, where f =1/1.2 since weight ratio of D:A= 1:1.2) of the dielectric constants of neat PTOBDT (ε_r = 4.21) and Y6 films (ε_r = 3.89).

Since dielectric constants of the blends could not account for the observed differences, Mott-Schottky analysis was done to measure the built-in potential to account for the V_{OC} and FF changes. The obtained values (from 4 devices to account for processing variations) are presented in **Figure 19** and **Table 9**. The built-in potential changes significantly upon annealing and addition of DIO additive:

Effect of annealing: V_{bi} decreased from 0.802 V (ND-RT) to 0.727 V upon annealing at 130 °C (ND-130C), and thus correlating with an increase in V_{OC}, while the increase in FF could be attributed to an increase in order/crystallinity (Y6 showed larger redshift upon annealing as compared to PTOBDT, in **Figure 14**c and d). On the other hand, for the DIO based devices, FF was similar in both the annealed (D-130C) and as-cast device (D-RT), so little direct dependence of FF on V_{bi} could be found, while V_{OC} increased with an increase in $V_{bi.}$

Effect of DIO additive: For the DIO additive-based devices, the V_{bi} was comparatively low: V_{bi} of 0.685 and 0.617 V was found for the as-cast (D-RT), annealed device (D-130C), respectively, vs 0.802 and 0.717 V for ND-RT and ND-130C, respectively. The lower V_{bi} values in DIO additive-based devices account for lower $V_{OC.}$

3.3.3 **Morphology characterization: AFM and surface tension measurement**

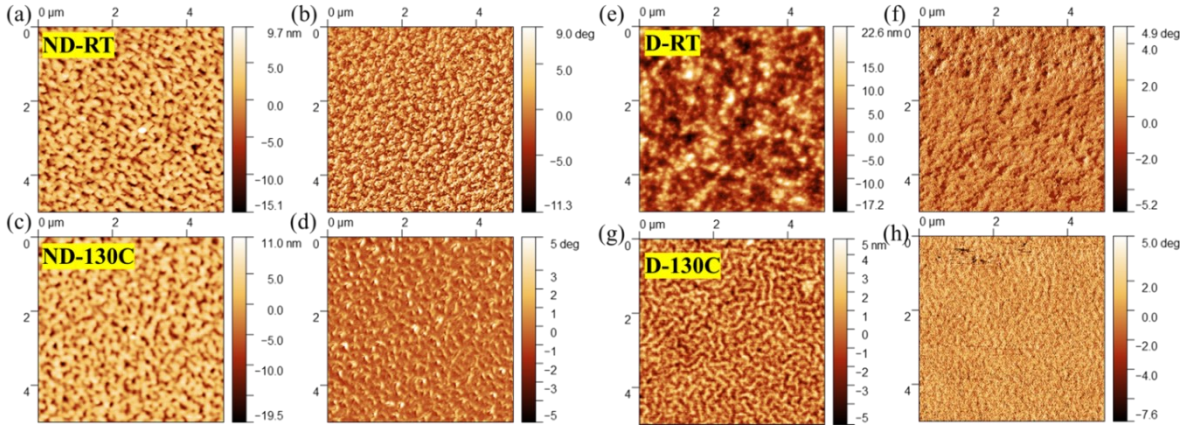

Figure 20 AFM images of PTOBDT:Y6 blend without/with DIO additive addition and without/with annealing: (a), (c), (e), and (g) are the height images; and (b) , (d), (f), and (h) are the phase images of blends without (ND-RT/ND-130C) and with (D-RT/D-130C) DIO additive, respectively.

The significantly different values of V_{bi} suggest a change in the morphological characteristics of the blend active layer, upon annealing/additive addition. AFM and surface energy measurements were carried out to analyze the morphological changes in the blends.

In without-DIO devices, the RMS roughness decreased from 8.34 nm (ND-RT) to 6.70 nm (ND-130C) upon annealing. Also, the RMS roughness decreased from 6.34 nm (D-RT) to 1.35 nm (D-130C) for DIO based devices upon annealing. A fiber-like structure appeared in the D-130C blend, which can suggest the polymer phase rearrangement (evidenced from an increase in the SCLC hole only mobility as compared to the annealed device without DIO (ND-130C)). Similar rearrangement (network formation) but to a smaller extent could be seen in the annealed without-DIO device (ND-130C) as compared to the as-cast device (ND-RT). These observations (**Figure 20**) point to redistribution of donor:acceptor domains in the blend.

However, PLQE was still maintained, therefore, the nanoscale phase separation could still be expected.

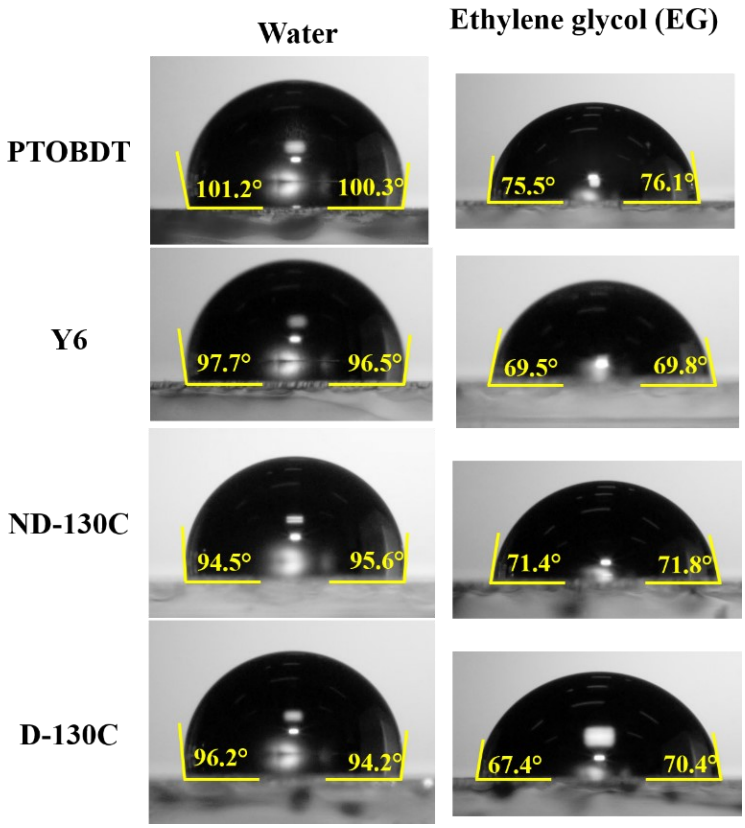

Figure 21 Contact angle of neat and blend films with water and EG as the probe liquids. Average of four angles (two angles per droplet) were taken; only one droplet is shown here.

Contact selectivity of donor/acceptor plays an important role in the overall device efficiency: donor polymer near anode contact (MoO_x) and acceptor molecules near cathode contact (ZnO) is preferred. Here, since cathode/anode contacts are the same, the processing condition is likely to change the degree to which the active layer/cathode interface is covered by acceptor molecules (Y6) and vice versa for anode contact. The morphology change was obvious from

the AFM images. Surface energy values can serve as an additional tool to characterize the relative change in the donor/acceptor coverage on the surface of the blend film and hence to characterize the contact selectivity. The contact angles with the two probe liquids, water and glycerol, and calculated surface tension values are shown in **Figure 21** and **Table 10**, respectively for the annealed devices. PTOBDT polymer has slightly lower surface tension than that of Y6. The surface energy of blend without additive (ND-130C) falls between that of the donor and acceptor, which is consistent with the theory of mixing (averaging) of surface energies and thus a homogenously mixed surface area. At the same time, the surface energy of blend with the additive (D-130C) is higher than both acceptor and donor. In conclusion, even though the surface energy of the blend changes on DIO addition, suggesting a vertical redistribution of donor and acceptor (V_{bi} changes suggest vertical stratification[47]), the surface energy values are too close to definitely tell if the donor domains preferably came on the top when DIO was added or vice versa.

Table 10 Contact angle and surface tension of neat and blend films.

	Contact angle* **(water) [°]**	**Contact angle*** **(EG) [°]**	**γ_p [mN/m]**	**γ_d [mN/m]**	**Surface tension, γ [mN/m]**
Neat films					
Y6	96.8	69.8	7.04	17.86	24.90
PTOBDT	100.7	75.1	5.86	16.87	22.73
PTOBDT:Y6 blend films					
ND-130C	95.0	71.1	9.21	14.70	23.91
D-130C	95.8	67.9	7.12	18.76	25.88

*Average of 4 angle measurements

Key: PTOBDT:Y6 blends with different processing conditions: ND-RT: without DIO and as cast; ND-130C: without DIO and annealed at 130 °C; D-RT: with DIO and as cast; D-130C: with DIO and annealed at 130 °C.

3.3.4 **Summary of Part I**

In summary, both annealing and DIO addition led to a significant change in the morphology of the blend, which is supported by the large V_{bi} changes and the proportional change in V_{OC}. Moreover, the narrowing of the bandgap in the DIO additive based devices (both D-RT and D-130C) might have also contributed to the decrease in $V_{OC.}$

Dielectric constants of the blends did not change unexpectedly higher/lower (with annealing or DIO additive addition) than the weighted average of donor and acceptor dielectric constants, therefore, not contributing directly to the P_{diss}, FF, and V_{OC} change.

3.4 Results and discussion: Part II- Effect of material properties: fluorination of donor polymer

3.4.1 **Photovoltaic performance**

Inverted device structure was used to fabricate OSC devices based on two polymer donors (a non-fluorinated, PBDTTh-TA, and a fluorinated PBDTThF-TA) and two acceptors (non-fluorinated ITIC and fluorinated IT-4F). The chemical structures, energy level alignment, and absorption spectra of neat and blend films are shown in **Figure 22**. OSC based on PBDTTh-TA:ITIC and PBDTThFF-TA:IT-4F showed the best and comparable PCEs (9.95% and 9.85%, respectively). PBDTTh-TA:IT-4F device showed slightly lower but modest PCE of 8.77%, mainly due to the lower V_{OC} compared to PBDTTh-TA:ITIC, which was expected since the LUMO of IT-4F lies lower than that of ITIC (**Figure 22**b). The device based on PBDTThF-TA:ITIC showed the worst performance with the lowest J_{SC} and FF among the four blend systems, although with the highest V_{OC} (as expected according to the $LUMO_A$ and $HOMO_D$ energy levels). Therefore, the trend of Voc correlates with the $HOMO_D$-$LUMO_A$ difference.

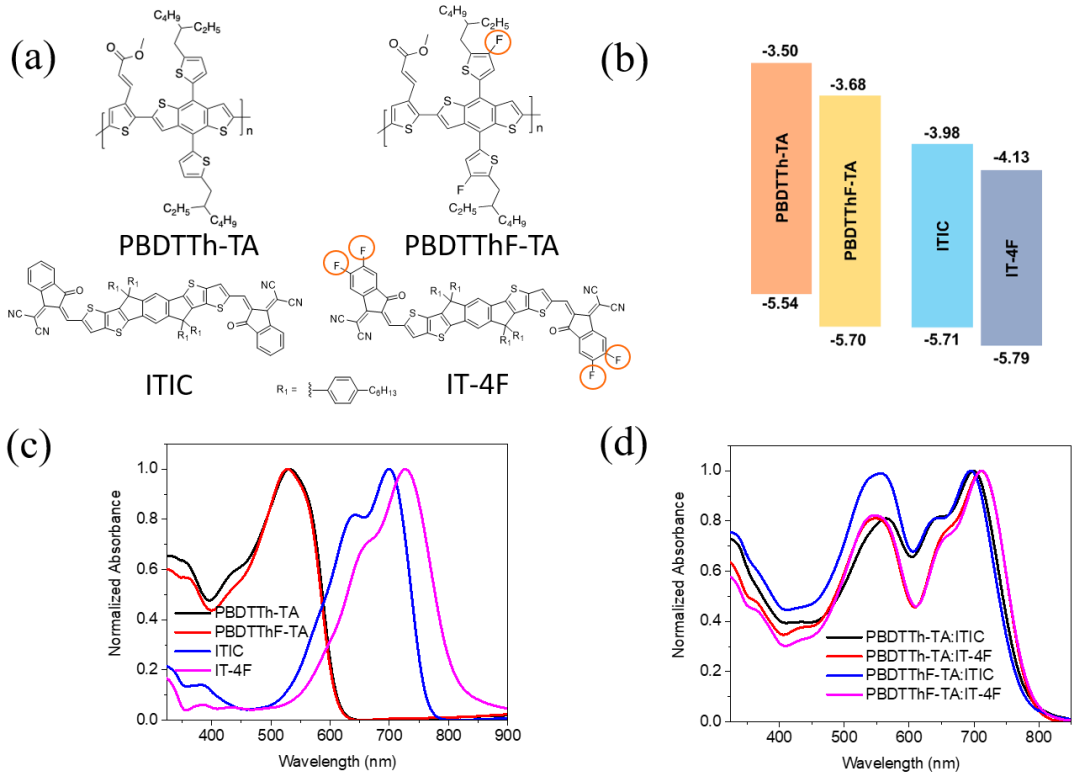

Figure 22 (a) Chemical structures of non-fluorinated and fluorinated donors and acceptors (F atoms are circled); (b) frontier energy levels of donors and acceptors; UV-vis spectra of (c) neat, and (d) blend films.

To analyze the trend of J_{SC}, a similar analysis was done as in the PTOBDT:Y6 system for quantifying exciton dissociation and charge collection efficiency. The device based on PBDTThF-TA:ITIC showed the lowest P_{diss} and P_{coll} of 74.33% and 44.05%, respectively (**Figure 24** and **Table 11**). Higher Jsc in IT-4F-based devices is contributed by the increased number of photons absorbed in the BHJ film showing an extended absorption with an EQE onset at ~805 nm (versus the onset of ~776 nm with ITIC, shown in **Figure 23**b). TF:TA devices did not reach a saturated J_{ph}, which is a signature of the low charge generation and collection efficiency of the blend.

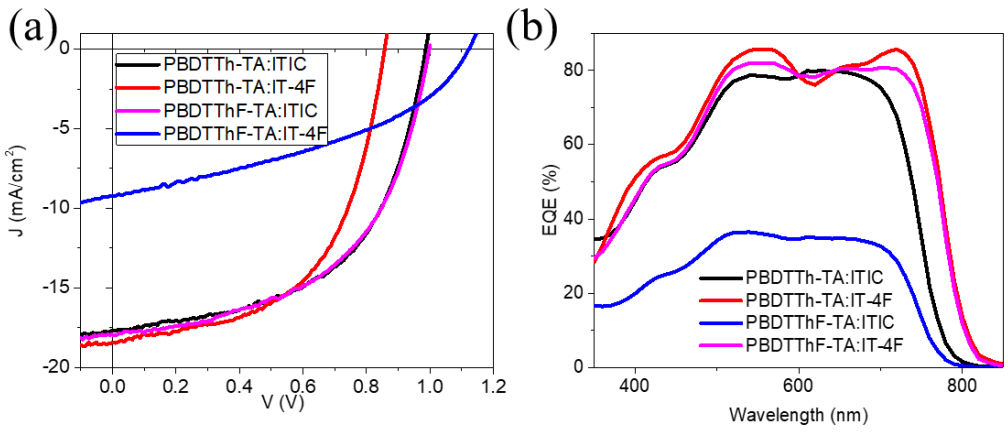

Figure 23 (a) J-V curve and (b) EQE spectra of OSCs based on fluorinated/non-fluorinated donor polymers and acceptors.

Table 11 Photovoltaic performance parameters devices with PBDTTh-TA and PBDTThF-TA polymer donors (average values are shown in parentheses).

	J_{SC} [mA cm^{-2}]	Voc [V]	FF	PCE [%]	J_{sat} [mA cm^{-2}]	P_{diss} [%]	P_{coll} [%]
PBDTTh-TA:ITIC	18.13 (17.69)	0.99 (0.98)	0.55 (0.54)	9.83 (9.34)	19.14	92.04	67.13
PBDTTh-TA:IT-4F	18.31 (18.24)	0.86 (0.86)	0.56 (0.55)	8.77 (8.67)	19.71	92.63	70.75
PBDTThF-TA:ITIC	9.21 (9.06)	1.12 (1.12)	0.40 (0.39)	4.10 (3.96)	11.75	74.33	44.05
PBDTThF-TA:IT-4F	19.84 (19.53)	1.00 (1.00)	0.50 (0.48)	9.95 (9.45)	19.03	91.29	67.75

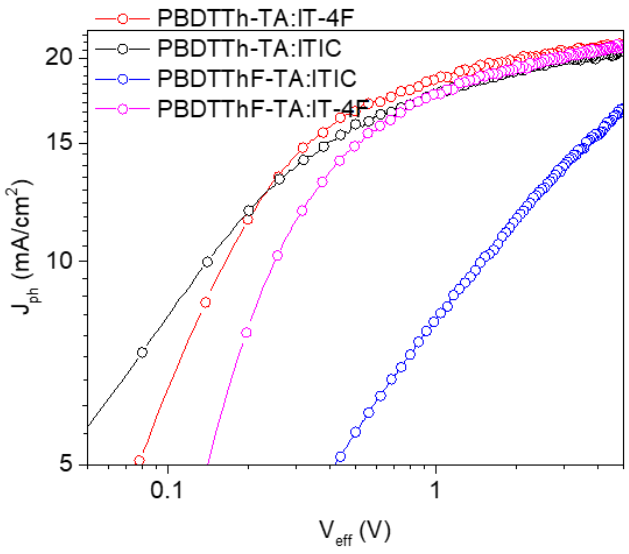

Figure 24 Photocurrent vs Effective voltage.

Donor PL was quenched effectively in all the blend systems, suggesting an efficient transfer of electrons from donor to the acceptor (and a nanoscale polymer domain size). However, the other channel (hole transfer from acceptor to donor) was severely limited in PBDTThF-TA:ITIC blend and hence the lowest J_{SC} (**Figure 25** and **Table 12** This observation is consistent with the fact that the HOMO offset is the minimum (0.01 eV) in this blend (**Figure 22**b).

It can be reasonably argued therefore that the donor and acceptors mixed intimately to form a nanoscale morphology in the three systems and for the PBDTThF-TA:ITIC system, either there was a lack of nanoscale mixing or ΔHOMO was not sufficient. Both these possibilities will be verified with SCLC mobility and morphology characterizations.

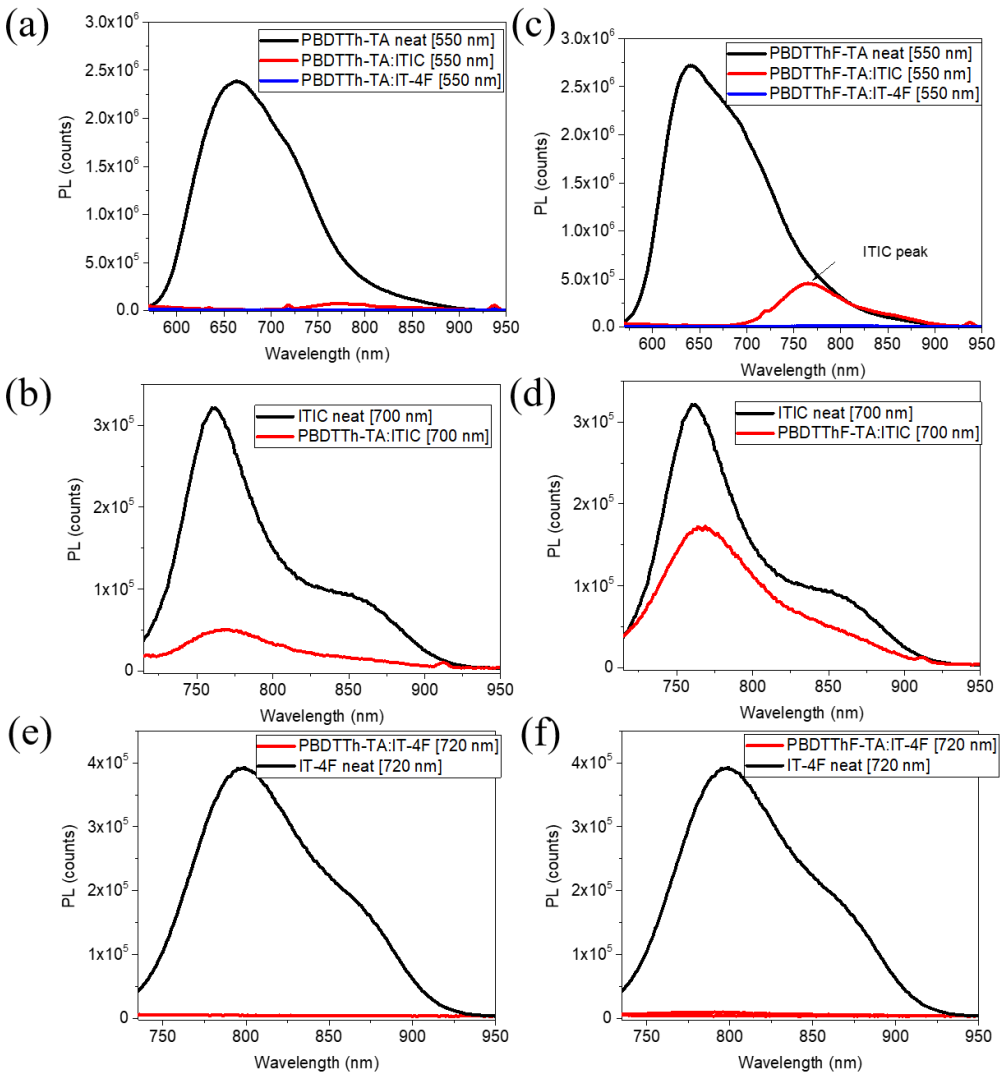

Figure 25 PL quenching of (a) Donor excitation of PBDTTh-TA (b) Donor excitation of PBDTThF-TA; (c) and (d): ITIC PL quenching by PBDTTh-TA and PBDTThF-TA, respectively; (e) and (f): IT-4F PL quenching by PBDTTh-TA and PBDTThF-TA, respectively.

Table 12 PL quenching data for blends.

	$PLQE_D$ [%]	**$PLQE_A$ [%]**
PBDTTh-TA:ITIC	98.9	92.4
PBDTTh-TA:IT-4F	99.8	99.7
PBDTThF-TA:ITIC	98.9	39.9
PBDTThF-TA:IT-4F	98.9	98.6

SCLC mobilities were measured to account for the charge transport limitation (if any) and comparatively analyze the low FF values in relation to mobility values (see **Figure 26** and **Table 13**). PBDTTh-TA:IT-4F device showed the most balanced $\mu_{electron}$ and μ_{hole} values, evident in the highest FF. Noticeably, all the blends showed lower SCLC electron mobilities compared to the respective neat acceptor films (in **Table 2**, ITIC: 1.6×10^{-4} vs IT-4F: 5.8×10^{-4} cm^2 V^{-1} s^{-1}) and thus limited charge collection efficiency (low FFs). The reduction in respective hole mobilities was less drastic.

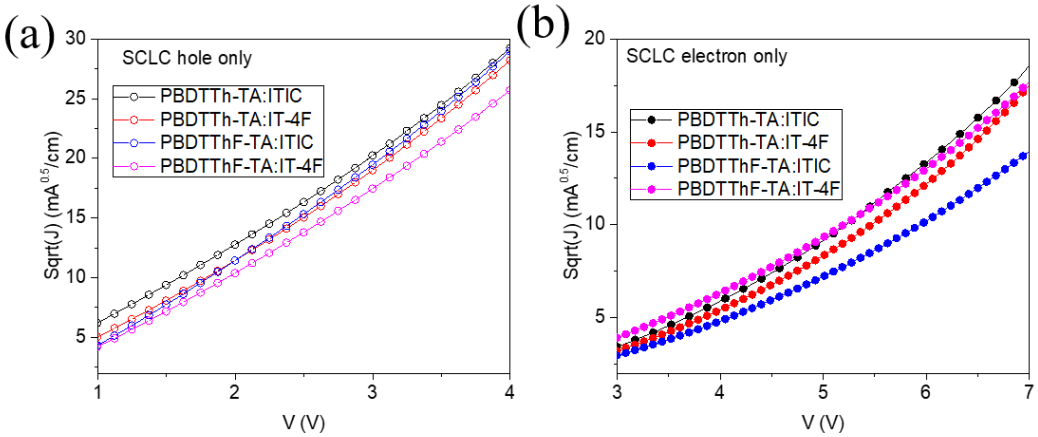

Figure 26 SCLC plots of blend films: (a) Hole only and (b) Electron only.

Table 13 SCLC mobilities of blend films.

	μ_{hole} [$\times 10^{-4}$ cm^2 V^{-1} s^{-1}]	$\mu_{electron}$ [$\times 10^{-4}$ cm^2 V^{-1} s^{-1}]	$\mu_{hole}/\mu_{electron}$
PBDTTh-TA:ITIC	1.09 ± 0.23	0.60 ± 0.10	1.82
PBDTTh-TA:IT-4F	0.80 ± 0.13	0.53 ± 0.10	1.51
PBDTThF-TA:ITIC	0.76 ± 0.26	0.32 ± 0.04	2.37
PBDTThF-TA:IT-4F	0.83 ± 0.53	0.43 ± 0.11	1.93

3.4.2 **Morphology characterization: AFM and surface tension measurement**

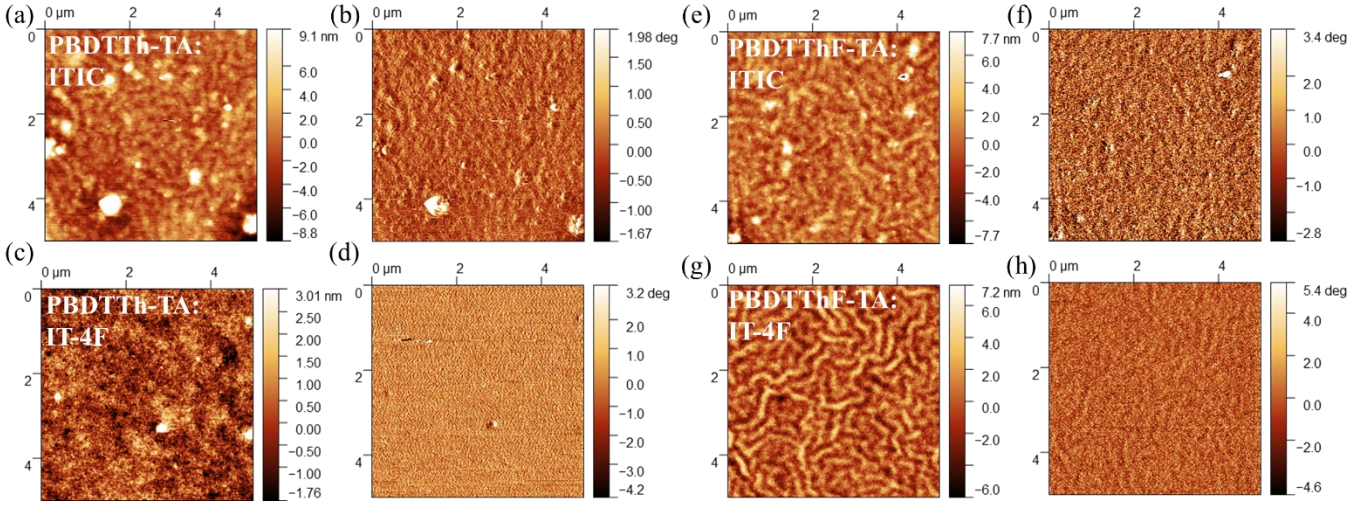

Figure 27 AFM height images of active layer blends of (a) PBDTTh-TA:ITIC, (c) PBDTTh-TA:IT-4F, (e) PBDTThF-TA:ITIC, and (g) PBDTThF-TA:IT-4F and AFM phase images of active layer blends of (b) PBDTTh-TA:ITIC, (d) PBDTTh-TA:IT-4F, (f) PBDTThF-TA:ITIC, and (h) PBDTThF-TA:IT-4F. All images were taken on 5 μm × 5 μm area.

Surface morphologies of the active layer blends were characterized using AFM and RMS roughness values were calculated from the height images. PBDTTh-TA:ITIC **(Figure 27**a and b) and PBDTThF:IT-4F (**Figure 27**c and d) showed RMS roughness values of 3.80 and 0.92 nm, respectively. Aggregated domains of ~1 μm size can be seen in the PBDTTh-TA:ITIC blends, which mostly contribute to the increased RMS roughness values. PBDTThF-TA based D:A blends with ITIC (**Figure 27**e and f) and IT-4F (**Figure 27**g and h) NFAs showed similar roughness values of 1.15 and 1.66 nm, respectively. Also, a network-like formation was seen in PBDTThF based blends (in both height and phase images). These fiber-like formations (>100 nm in width) are usually attributed to aggregated domains. On the other hand, PBDTh-TA:IT-4F films displayed a relatively mixed morphology. It is clear from the AFM images that the four blends have very distinct morphologies. The fluorinated polymer PBDTThF-TA-based blends tend to aggregate, while the non-fluorinated polymer PBDTTh-TA based blends show moderate mixing.

In order to gain information about the relative miscibility (which could explain the loss in mobilities in blends compared to the neat films and the AFM morphology), miscibility analysis was done by calculating surface energy values (γ) of the donor polymers and NFAs and using those values in an empirical relation[53]:

$$\chi \propto \left(\sqrt{\gamma_{donor}} - \sqrt{\gamma_{acceptor}}\right)^2 \qquad 3.2$$

The relative χ values can predict the extent of miscibility. The measured contact angles and calculated values of $\left(\sqrt{\gamma_{donor}} - \sqrt{\gamma_{acceptor}}\right)^2$ are shown in **Figure 28** and **Table 14**.

According to the relative miscibility values, PBDTTh-TA:ITIC would form the most intensely mixed system, while PBDTThF-TA:IT-4F system could be predicted to have the least intermixing. At the same time, it is evident from the PL results that the mixing is good enough for forming nanoscale domains and hence efficient exciton dissociation in PBDTThF-TA:IT-4F, despite the lowest miscibility.

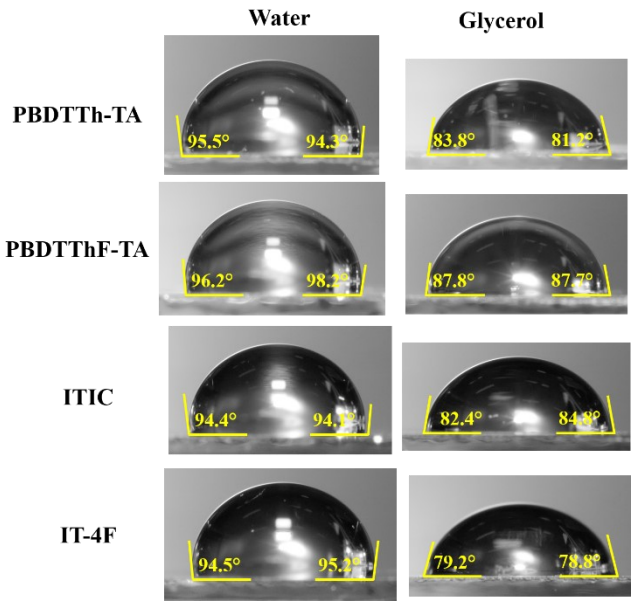

Figure 28 Contact angles of water and glycerol as probe liquids on neat films.

It follows from it that the mobility reduction in the PBDTThF-TA:IT-4F would be the minimum. Noticeably, $\left(\sqrt{\gamma_{donor}} - \sqrt{\gamma_{acceptor}}\right)^2$ values are much lower than the reported values for most high performing systems in literature.[31–33,107] Therefore, too-mixed phases (of donor and acceptors) might be present in all the systems discussed in this part and the low acceptor part $PLQE_A$ in PBDTThF-TA:ITIC blend might be primarily due to the insufficient HOMO offset.

Table 14 Surface tension and interaction parameter of polymer donors and acceptors.

	Contact angle* (water) [°]	**Contact angle* (glycerol) [°]**	**γ_p [mN/m]**	**γ_d [mN/m]**	**Surface tension, γ [mN/m]**	$\left(\sqrt{\gamma_{donor}} - \sqrt{\gamma_{acceptor}}\right)^2$
ITIC	94.2	83.6	9.34	15.09	24.43	
IT-4F	94.7	78.9	6.57	21.54	28.11	
PBDTTh-TA	94.9	82.5	8.12	17.14	25.26	
PBDTThF-TA	96.8	87.7	9.31	12.95	22.25	
PBDTTh-TA:ITIC						0.01
PBDTTh-TA:IT-4F						0.08
PBDTThF-TA:ITIC						0.05
PBDTThF-TA:IT-4F						0.34
*Average of 4 values						

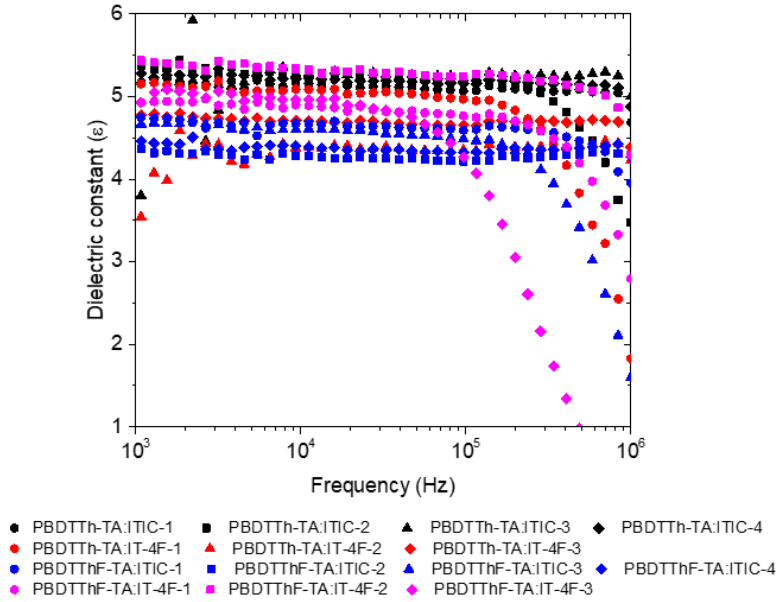

Figure 29 Dielectric constant of blends.

3.4.3 **Dielectric constant of blends and built-in potential**

The dielectric constants obtained at 10 kHz are also shown in **Table 15** and the frequency variation of blend dielectric constants is shown in **Figure 29**. It had been reported that fluorination would increase the dielectric constant of the neat films (consistent with the values in **Table 5**) and hence that of the blend. Blends based on PBDTTh-TA:ITIC showed the highest ε_{blend} of 5.24, which contrasts with the theory that fluorination of donor/acceptor will increase the dielectric constant of the blend. It is therefore important to consider the effects of molecular arrangements in predicting the dielectric constant of a mixed system,[92] unlike the simple theory of mixing commonly used for calculating the dielectric constant of blends using the dielectric constant values of the neat donor and acceptor (Section 1.3.7). Both fluorinated donor and fluorinated acceptor (with a higher dielectric constant than that of the fluorinated counterpart) might not lead to a blend with a higher dielectric constant than that based on non-fluorinated donor/acceptor. Also, small changes in the dielectric constant might not lead to observable changes in the device performance, if the energy level offsets and SCLC mobilities are low.[102] A direct correlation, therefore, was not found for either $P_{diss,}$ FF or V_{OC} with respective dielectric constants of the four systems.

Mott-Schottky plot was used to calculate the built-in potential (V_{bi}) of the four blend systems to account for the V_{OC} losses (**Figure 30** and **Table 15**). Since the device structure was similar, it should be expected that the V_{bi} should be similar, if one considers the work function difference as the only contributor to the internal electric field. Several previous reports have defined the V_{in} in a similar way (Section 1.3.8)[42]. However, a clear correlation could be observed for the energy loss ($E_{loss} = E_g - qV_{OC}$) and V_{bi}. The E_{loss} was minimum for the device with the maximum V_{bi} (PBDTThF-TA:ITIC), although the overall performance was the lowest. Since the HOMO/LUMO levels are different for the four combinations, a direct comparison of V_{OC} would not be useful.

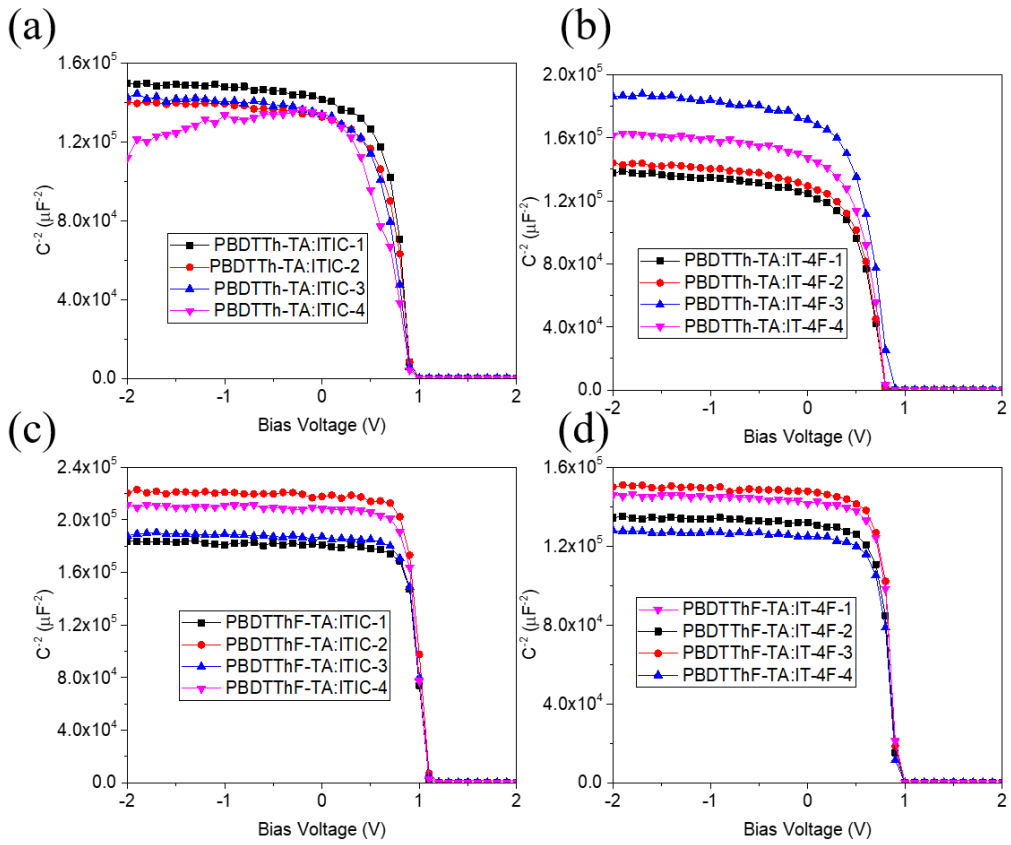

Figure 30 Mott-Schottky plot of (a) PBDTTh-TA:ITIC; (b) PBDTTh-TA:IT-4F; (c) PBDTThF-TA:ITIC; (d) PBDTThF-TA:IT-4F blends. Four devices for each blend were analyzed for reliable comparisons.

Table 15 Dielectric constant, V_{bi}, and V_{oc} loss data.

	V_{bi} [V]	**ε_r**	**E_g/q-V_{OC} [V]**
PBDTTh-TA:ITIC	0.91 ± 0.004	5.24 ± 0.05	0.624
PBDTTh-TA:IT-4F	0.80 ± 0.025	4.80 ± 0.28	0.656
PBDTThF-TA:ITIC	1.08 ± 0.004	4.49 ± 0.16	0.494
PBDTThF-TA:IT-4F	0.92 ± 0.007	5.05 ± 0.17	0.516

3.4.4 **Summary of Part II**

Fluorinated polymer blended with fluorinated acceptor did not achieve the highest dielectric constant among the four blends. Moreover, direct correlations between dielectric constants on device parameters were not visible possibly because of the significantly different morphology.

Fluorinated polymer (PBDTThF-TA) has a larger E_b than the non-fluorinated polymer (PBDTTh-TA), but the PBDTThF-TA:IT-4F blend showed efficient exciton dissociation or charge transfer efficiency, because of sufficient energy level offsets and PL quenching.

It is worth mentioning here that these results represent only a few combinations from several possible device optimization matrices with varying processing conditions: different thermal annealing temperatures, solvent annealing, D:A ratios, etc. Therefore, even for the same D:A combinations studied in both Part I and Part II, the observations might differ significantly if the processing conditions are changed. The aim of this chapter of the thesis is to show that several parameters interact together in an OSC and we should be careful to account for them while studying the effect of dielectric constant on device performance.

Chapter 4
Summary and future directions

The dielectric constants of neat polymer donor films lie in the range 3-5, even with significant differences in the polymer backbones. This is probably because the elemental variations (apart from the addition of F) are very low among these polymers and therefore the resulting permanent dipole moments do not change significantly. The exciton binding energies of the polymer donors are not necessarily inversely proportional to the dielectric constant.

In the blends, variations in processing conditions can lead to significant differences in the photovoltaic performance of OSCs, without appreciable changes in the dielectric constant. The effects of morphology and molecular energy level alignment in donor:acceptor blend can subdue the change in the dielectric constant of the blend. Therefore, designing a polymer donor with an exclusive target to increase the dielectric constant might not be useful because of the dominance of other parameters crucial to the device performance.

From Chapter 2, it can be concluded that attempts to increase the dielectric constant with an aim to decrease the E_b might not be the right direction. We should note that exciton formation is not a bulk phenomenon but rather an intramolecular process, and therefore E_b cannot always be correlated directly with the bulk dielectric constant values.

From chapter 3, it can be concluded that small changes in dielectric constants of the blends (by changing the processing conditions or component materials' dielectric constants) might not lead to appreciable changes in the OSC performances, especially when the competing parameters like energy level alignments and morphology change significantly. In addition, when the differences in the dielectric constants are small, the study of the influence of dielectric constant on device performance becomes rather complicated.

Future directions:

- A systemic investigation on the effect of dipole moment and dielectric constant on E_b of polymer donors can be done:

- The dipole moment calculation for the excited states and with multiple monomer units should be done. This would provide a closer picture of the polarizability of the excited state along with the influence of inter/intramolecular delocalization.
- The electron-hole separation distance, r is one of the main unknowns in exciton binding energy calculation and is related to the inter/intramolecular delocalization. Therefore, the extent of molecular packing (2D/3D) can provide more insight into the cumulative effect of both dielectric constant and electron-hole separation distance on the exciton binding energy in the polymer donor films.

- In the blends, the donor/acceptor relative miscibility, crystallinity (and crystal size), molecular packing, etc. can be further probed via synchrotron grazing incidence wide-angle x-ray spectroscopy (GIWAXS), transmission electron microscopy (TEM), and so on. With a better clarity of the donor/acceptor packing in blend films and thus the effective dipole direction, the dielectric constant of the blends can be predicted with better accuracy.

Bibliography

1. Liu, Q., Jiang, Y., Jin, K., Qin, J., Xu, J., Li, W., Xiong, J., Liu, J., Xiao, Z., Sun, K., Yang, S., Zhang, X., & Ding, L. (2020). 18% Efficiency organic solar cells. *Science Bulletin*, *65*(4), 272–275. https://doi.org/10.1016/j.scib.2020.01.001

2. Lin, Y., Adilbekova, B., Firdaus, Y., Yengel, E., Faber, H., Sajjad, M., Zheng, X., Yarali, E., Seitkhan, A., Bakr, O. M., El-Labban, A., Schwingenschlögl, U., Tung, V., McCulloch, I., Laquai, F., & Anthopoulos, T. D. (2019). 17% Efficient Organic Solar Cells Based on Liquid Exfoliated WS2 as a Replacement for PEDOT:PSS. *Advanced Materials*, *31*(46), 1902965. https://doi.org/10.1002/adma.201902965

3. Jiang, K., Wei, Q., Lai, J. Y. L., Peng, Z., Kim, H. K., Yuan, J., Ye, L., Ade, H., Zou, Y., & Yan, H. (2019). Alkyl Chain Tuning of Small Molecule Acceptors for Efficient Organic Solar Cells. *Joule*, *3*(12), 3020–3033. https://doi.org/10.1016/j.joule.2019.09.010

4. Green, M. A., Dunlop, E. D., Hohl-Ebinger, J., Yoshita, M., Kopidakis, N., & Hao, X. (2020). Solar cell efficiency tables (version 56). *Progress in Photovoltaics: Research and Applications*, *28*(7), 629–638. https://doi.org/10.1002/pip.3303

5. Shockley, W., & Queisser, H. J. (1961). Detailed Balance Limit of Efficiency of p-n Junction Solar Cells. *Journal of Applied Physics*, *32*(3), 510–519. https://doi.org/10.1063/1.1736034

6. Hou, J., Inganäs, O., Friend, R. H., & Gao, F. (2018). Organic solar cells based on non-fullerene acceptors. *Nature Materials*, *17*(2), 119–128. https://doi.org/10.1038/nmat5063

7. Jeong, M., Choi, I. W., Go, E. M., Cho, Y., Kim, M., Lee, B., Jeong, S., Jo, Y., Choi, H. W., Lee, J., Bae, J.-H., Kwak, S. K., Kim, D. S., & Yang, C. (2020). Stable perovskite solar cells with efficiency exceeding 24.8% and 0.3-V voltage loss. *Science*, *369*(6511), 1615. https://doi.org/10.1126/science.abb7167

8. Ji, Y., Xu, L., Hao, X., & Gao, K. (2020). Energy Loss in Organic Solar Cells: Mechanisms, Strategies, and Prospects. *Solar RRL*, *4*(7), 2000130. https://doi.org/10.1002/solr.202000130

9. Chen, Z.-H., Bi, P.-Q., Yang, X.-Y., Niu, M.-S., Zhang, K.-N., Feng, L., & Hao, X.-T. (2019). Quantitatively Characterized Crystallization Effect on Recombination Energy Loss in Non-Fullerene Organic Solar Cells. *The Journal of Physical Chemistry C*, *123*(20), 12676–12683. https://doi.org/10.1021/acs.jpcc.9b03572

10. Forrest, S. R. (2005). The Limits to Organic Photovoltaic Cell Efficiency. *MRS Bulletin*, *30*(1), 28–32. https://doi.org/10.1557/mrs2005.5

11. Kippelen, B., & Brédas, J.-L. (2009). Organic photovoltaics. *Energy & Environmental Science*, *2*(3), 251–261. https://doi.org/10.1039/B812502N

12. Gregg, B. A. (2003). Excitonic Solar Cells. *The Journal of Physical Chemistry B*, *107*(20), 4688–4698. https://doi.org/10.1021/jp022507x

13. Kim, H. K. (2018). *Work function tuning of electrode materials with small molecule surface modifiers*. https://smartech.gatech.edu/handle/1853/60270

14. Clarke, T. M., & Durrant, J. R. (2010). Charge Photogeneration in Organic Solar Cells. *Chemical Reviews*, *110*(11), 6736–6767. https://doi.org/10.1021/cr900271s

15. Deibel, C., & Dyakonov, V. (2010). Polymer–fullerene bulk heterojunction solar cells. *Reports on Progress in Physics*, *73*(9), 096401. https://doi.org/10.1088/0034-4885/73/9/096401

16. Kang, H., Kim, G., Kim, J., Kwon, S., Kim, H., & Lee, K. (2016). Bulk-Heterojunction Organic Solar Cells: Five Core Technologies for Their Commercialization. *Advanced Materials*, *28*(36), 7821–7861. https://doi.org/10.1002/adma.201601197

17. Ganesan, S., Mehta, S., & Gupta, D. (2019). Fully printed organic solar cells – a review of techniques, challenges and their solutions. *Opto-Electronics Review*, *27*(3), 298–320. https://doi.org/10.1016/j.opelre.2019.09.002

18. Wang, G., Adil, M. A., Zhang, J., & Wei, Z. (2019). Large-Area Organic Solar Cells: Material Requirements, Modular Designs, and Printing Methods. *Advanced Materials*, *31*(45), 1805089. https://doi.org/10.1002/adma.201805089

19. Xue, R., Zhang, J., Li, Y., & Li, Y. (2018). Organic Solar Cell Materials toward Commercialization. *Small*, *14*(41), 1801793. https://doi.org/10.1002/smll.201801793

20. Firdaus, Y., Corre, V. M. L., Khan, J. I., Kan, Z., Laquai, F., Beaujuge, P. M., & Anthopoulos, T. D. (2019). Key Parameters Requirements for Non-Fullerene-Based Organic Solar Cells with Power Conversion Efficiency >20%. *Advanced Science*, *6*(9), 1802028. https://doi.org/10.1002/advs.201802028

21. Proctor, C. M., Kuik, M., & Nguyen, T.-Q. (2013). Charge carrier recombination in organic solar cells. *Progress in Polymer Science*, *38*(12), 1941–1960. https://doi.org/10.1016/j.progpolymsci.2013.08.008

22. Gusain, A., Faria, R. M., & Miranda, P. B. (2019). Polymer Solar Cells—Interfacial Processes Related to Performance Issues. *Frontiers in Chemistry*, *7*(61). https://doi.org/10.3389/fchem.2019.00061

23. Sze, S. M., & Ng, K. K. (2006). *Physics of Semiconductor Devices*. John Wiley & Sons.

24. Collins, S. D., Proctor, C. M., Ran, N. A., & Nguyen, T.-Q. (2016). Understanding Open-Circuit Voltage Loss through the Density of States in Organic Bulk Heterojunction Solar Cells. *Advanced Energy Materials*, *6*(4), 1501721. https://doi.org/10.1002/aenm.201501721

25. Veldman, D., İpek, Ö., Meskers, S. C. J., Sweelssen, J., Koetse, M. M., Veenstra, S. C., Kroon, J. M., van Bavel, S. S., Loos, J., & Janssen, R. A. J. (2008). Compositional and Electric Field Dependence of the Dissociation of Charge Transfer Excitons in Alternating Polyfluorene Copolymer/Fullerene Blends. *Journal of the American Chemical Society*, *130*(24), 7721–7735. https://doi.org/10.1021/ja8012598

26. Qi, B., & Wang, J. (2013). Fill factor in organic solar cells. *Physical Chemistry Chemical Physics*, *15*(23), 8972–8982. https://doi.org/10.1039/C3CP51383A

27. Leilaeioun, M., & Holman, Z. C. (2016). Accuracy of expressions for the fill factor of a solar cell in terms of open-circuit voltage and ideality factor. *Journal of Applied Physics*, *120*(12), 123111. https://doi.org/10.1063/1.4962511

28. Bredas, J.-L. (2013). Mind the gap! *Materials Horizons*, *1*(1), 17–19. https://doi.org/10.1039/C3MH00098B

29. Ziffer, M. E., Jo, S. B., Zhong, H., Ye, L., Liu, H., Lin, F., Zhang, J., Li, X., Ade, H. W., Jen, A. K.-Y., & Ginger, D. S. (2018). Long-Lived, Non-Geminate, Radiative

Recombination of Photogenerated Charges in a Polymer/Small-Molecule Acceptor Photovoltaic Blend. *Journal of the American Chemical Society*, *140*(31), 9996–10008. https://doi.org/10.1021/jacs.8b05834

30. Baran, D., Gasparini, N., Wadsworth, A., Tan, C. H., Wehbe, N., Song, X., Hamid, Z., Zhang, W., Neophytou, M., Kirchartz, T., Brabec, C. J., Durrant, J. R., & McCulloch, I. (2018). Robust nonfullerene solar cells approaching unity external quantum efficiency enabled by suppression of geminate recombination. *Nature Communications*, *9*(1), 2059. https://doi.org/10.1038/s41467-018-04502-3

31. Ye, L., Li, S., Liu, X., Zhang, S., Ghasemi, M., Xiong, Y., Hou, J., & Ade, H. (2019). Quenching to the Percolation Threshold in Organic Solar Cells. *Joule*, *3*(2), 443–458. https://doi.org/10.1016/j.joule.2018.11.006

32. Liang, Z., Li, M., Wang, Q., Qin, Y., Stuard, S. J., Peng, Z., Deng, Y., Ade, H., Ye, L., & Geng, Y. (2020). Optimization Requirements of Efficient Polythiophene:Nonfullerene Organic Solar Cells. *Joule*, *4*(6), 1278–1295. https://doi.org/10.1016/j.joule.2020.04.014

33. Jeon, S. J., Han, Y. W., Kim, Y. H., & Moon, D. K. (2020). Case Study on the Correlation between Crystal Packing and Miscibility of Chlorinated Thiophene–Based Donor Polymers for Nonfullerene Organic Solar Cells with Long Shelf Life. *Solar RRL*, *4*(7), 2000074. https://doi.org/10.1002/solr.202000074

34. Yi, N., Ai, Q., Zhou, W., Huang, L., Zhang, L., Xing, Z., Li, X., Zeng, J., & Chen, Y. (2019). Miscibility Matching and Bimolecular Crystallization Affording High-

Performance Ternary Nonfullerene Solar Cells. *Chemistry of Materials*, *31*(24), 10211–10224. https://doi.org/10.1021/acs.chemmater.9b03935

35. Ghasemi, M., Hu, H., Peng, Z., Rech, J. J., Angunawela, I., Carpenter, J. H., Stuard, S. J., Wadsworth, A., McCulloch, I., You, W., & Ade, H. (2019). Delineation of Thermodynamic and Kinetic Factors that Control Stability in Non-fullerene Organic Solar Cells. *Joule*, *3*(5), 1328–1348. https://doi.org/10.1016/j.joule.2019.03.020
36. Mark, P., & Helfrich, W. (1962). Space-Charge-Limited Currents in Organic Crystals. *Journal of Applied Physics*, *33*(1), 205–215. https://doi.org/10.1063/1.1728487
37. Malliaras, G. G., Salem, J. R., Brock, P. J., & Scott, C. (1998). Electrical characteristics and efficiency of single-layer organic light-emitting diodes. *Physical Review B*, *58*(20), R13411–R13414. https://doi.org/10.1103/PhysRevB.58.R13411
38. Fu, Z., Zhang, X., Zhang, H., Li, Y., Zhou, H., & Zhang, Y. (2021). On the Understandings of Dielectric Constant and Its Impacts on the Photovoltaic Efficiency in Organic Solar Cells. *Chinese Journal of Chemistry*. https://doi.org/10.1002/cjoc.202000289
39. Torabi, S., Jahani, F., Severen, I. V., Kanimozhi, C., Patil, S., Havenith, R. W. A., Chiechi, R. C., Lutsen, L., Vanderzande, D. J. M., Cleij, T. J., Hummelen, J. C., & Koster, L. J. A. (2015). Strategy for Enhancing the Dielectric Constant of Organic Semiconductors Without Sacrificing Charge Carrier Mobility and Solubility. *Advanced Functional Materials*, *25*(1), 150–157. https://doi.org/10.1002/adfm.201402244

40. Cho, N., Schlenker, C. W., Knesting, K. M., Koelsch, P., Yip, H.-L., Ginger, D. S., & Jen, A. K.-Y. (2014). High-Dielectric Constant Side-Chain Polymers Show Reduced Non-Geminate Recombination in Heterojunction Solar Cells. *Advanced Energy Materials*, *4*(10), 1301857. https://doi.org/10.1002/aenm.201301857

41. Hughes, M. P., Rosenthal, K. D., Ran, N. A., Seifrid, M., Bazan, G. C., & Nguyen, T.-Q. (2018). Determining the Dielectric Constants of Organic Photovoltaic Materials Using Impedance Spectroscopy. *Advanced Functional Materials*, *28*(32), 1801542. https://doi.org/10.1002/adfm.201801542

42. Sandberg, O. J., Kurpiers, J., Stolterfoht, M., Neher, D., Meredith, P., Shoaee, S., & Armin, A. (2020). On the Question of the Need for a Built-In Potential in Perovskite Solar Cells. *Advanced Materials Interfaces*, *7*(10), 2000041. https://doi.org/10.1002/admi.202000041

43. Vasilopoulou, M., Douvas, A. M., Georgiadou, D. G., Constantoudis, V., Davazoglou, D., Kennou, S., Palilis, L. C., Daphnomili, D., Coutsolelos, A. G., & Argitis, P. (2014). Large work function shift of organic semiconductors inducing enhanced interfacial electron transfer in organic optoelectronics enabled by porphyrin aggregated nanostructures. *Nano Research*, *7*(5), 679–693. https://doi.org/10.1007/s12274-014-0428-9

44. Manda, P. K., Ramaswamy, S., & Dutta, S. (2018). Extraction of the Built-in Potential for Organic Solar Cells From Current–Voltage Characteristics. *IEEE Transactions on Electron Devices*, *65*(1), 184–190. https://doi.org/10.1109/TED.2017.2773708

45. Kirchartz, T., Gong, W., Hawks, S. A., Agostinelli, T., MacKenzie, R. C. I., Yang, Y., & Nelson, J. (2012). Sensitivity of the Mott–Schottky Analysis in Organic Solar Cells. *The Journal of Physical Chemistry C*, *116*(14), 7672–7680. https://doi.org/10.1021/jp300397f

46. Duan, L., Meng, X., Zhang, Y., Yi, H., Jin, K., Haque, F., Xu, C., Xiao, Z., Ding, L., & Uddin, A. (2019). Comparative analysis of burn-in photo-degradation in non-fullerene COi8DFIC acceptor based high-efficiency ternary organic solar cells. *Materials Chemistry Frontiers*, *3*(6), 1085–1096. https://doi.org/10.1039/C9QM00130A

47. Han, J., Wang, Y., & Zhu, F. (2020). Built-In Potential and Operational Stability of Nonfullerene Organic Solar Cells. *Energy Technology*, *8*(12), 2000245. https://doi.org/10.1002/ente.202000245

48. Upama, M. B., Elumalai, N. K., Mahmud, M. A., Wright, M., Wang, D., Xu, C., & Uddin, A. (2018). Effect of annealing dependent blend morphology and dielectric properties on the performance and stability of non-fullerene organic solar cells. *Solar Energy Materials and Solar Cells*, *176*, 109–118. https://doi.org/10.1016/j.solmat.2017.11.027

49. Guerrero, A., Montcada, N. F., Ajuria, J., Etxebarria, I., Pacios, R., Garcia-Belmonte, G., & Palomares, E. (2013). Charge carrier transport and contact selectivity limit the operation of PTB7-based organic solar cells of varying active layer thickness. *Journal of Materials Chemistry A*, *1*(39), 12345–12354. https://doi.org/10.1039/C3TA12358H

50. Ye, L., Collins, B. A., Jiao, X., Zhao, J., Yan, H., & Ade, H. (2018). Miscibility–Function Relations in Organic Solar Cells: Significance of Optimal Miscibility in Relation to Percolation. *Advanced Energy Materials*, *8*(28), 1703058. https://doi.org/10.1002/aenm.201703058

51. Jiao, X., Ye, L., & Ade, H. (2017). Quantitative Morphology–Performance Correlations in Organic Solar Cells: Insights from Soft X-Ray Scattering. *Advanced Energy Materials*, *7*(18), 1700084. https://doi.org/10.1002/aenm.201700084

52. Xue, X., Weng, K., Qi, F., Zhang, Y., Wang, Z., Ali, J., Wei, D., Sun, Y., Liu, F., Wan, M., Liu, J., & Huo, L. (2019). Steric Engineering of Alkylthiolation Side Chains to Finely Tune Miscibility in Nonfullerene Polymer Solar Cells. *Advanced Energy Materials*, *9*(4), 1802686. https://doi.org/10.1002/aenm.201802686

53. Kouijzer, S., Michels, J. J., van den Berg, M., Gevaerts, V. S., Turbiez, M., Wienk, M. M., & Janssen, R. A. J. (2013). Predicting Morphologies of Solution Processed Polymer:Fullerene Blends. *Journal of the American Chemical Society*, *135*(32), 12057–12067. https://doi.org/10.1021/ja405493j

54. Comyn, J. (1992). Contact angles and adhesive bonding. *International Journal of Adhesion and Adhesives*, *12*(3), 145–149. https://doi.org/10.1016/0143-7496(92)90045-W

55. Yang, C., Zhang, J., Liang, N., Yao, H., Wei, Z., He, C., Yuan, X., & Hou, J. (2019). Effects of energy-level offset between a donor and acceptor on the photovoltaic performance of non-fullerene organic solar cells. *Journal of Materials Chemistry A*, *7*(32), 18889–18897. https://doi.org/10.1039/C9TA04789A

56. Li, S., Zhan, L., Sun, C., Zhu, H., Zhou, G., Yang, W., Shi, M., Li, C.-Z., Hou, J., Li, Y., & Chen, H. (2019). Highly Efficient Fullerene-Free Organic Solar Cells Operate at Near Zero Highest Occupied Molecular Orbital Offsets. *Journal of the American Chemical Society*, *141*(7), 3073–3082. https://doi.org/10.1021/jacs.8b12126

57. Yao, H., Cui, Y., Qian, D., Ponseca, C. S., Honarfar, A., Xu, Y., Xin, J., Chen, Z., Hong, L., Gao, B., Yu, R., Zu, Y., Ma, W., Chabera, P., Pullerits, T., Yartsev, A., Gao, F., & Hou, J. (2019). 14.7% Efficiency Organic Photovoltaic Cells Enabled by Active Materials with a Large Electrostatic Potential Difference. *Journal of the American Chemical Society*, *141*(19), 7743–7750. https://doi.org/10.1021/jacs.8b12937

58. Jakowetz, A. C., Böhm, M. L., Sadhanala, A., Huettner, S., Rao, A., & Friend, R. H. (2017). Visualizing excitations at buried heterojunctions in organic semiconductor blends. *Nature Materials*, *16*(5), 551–557. https://doi.org/10.1038/nmat4865

59. Gélinas, S., Rao, A., Kumar, A., Smith, S. L., Chin, A. W., Clark, J., Poll, T. S. van der, Bazan, G. C., & Friend, R. H. (2014). Ultrafast Long-Range Charge Separation in Organic Semiconductor Photovoltaic Diodes. *Science*, *343*(6170), 512–516. https://doi.org/10.1126/science.1246249

60. Gregg, B. A. (2011). Entropy of Charge Separation in Organic Photovoltaic Cells: The Benefit of Higher Dimensionality. *The Journal of Physical Chemistry Letters*, *2*(24), 3013–3015. https://doi.org/10.1021/jz2012403

61. Xu, Y., Yao, H., Ma, L., Wang, J., & Hou, J. (2020). Efficient charge generation at low energy losses in organic solar cells: A key issues review. *Reports on Progress in Physics*, *83*(8), 082601. https://doi.org/10.1088/1361-6633/ab90cf

62. Yuan, J., Huang, T., Cheng, P., Zou, Y., Zhang, H., Yang, J. L., Chang, S.-Y., Zhang, Z., Huang, W., Wang, R., Meng, D., Gao, F., & Yang, Y. (2019). Enabling low voltage losses and high photocurrent in fullerene-free organic photovoltaics. *Nature Communications*, *10*(1), 570. https://doi.org/10.1038/s41467-019-08386-9

63. Qian, D., Zheng, Z., Yao, H., Tress, W., Hopper, T. R., Chen, S., Li, S., Liu, J., Chen, S., Zhang, J., Liu, X.-K., Gao, B., Ouyang, L., Jin, Y., Pozina, G., Buyanova, I. A., Chen, W. M., Inganäs, O., Coropceanu, V., … Gao, F. (2018). Design rules for minimizing voltage losses in high-efficiency organic solar cells. *Nature Materials*, *17*(8), 703–709. https://doi.org/10.1038/s41563-018-0128-z

64. Hong, L., Yao, H., Yu, R., Xu, Y., Gao, B., Ge, Z., & Hou, J. (2019). Investigating the Trade-Off between Device Performance and Energy Loss in Nonfullerene Organic Solar Cells. *ACS Applied Materials & Interfaces*, *11*(32), 29124–29131. https://doi.org/10.1021/acsami.9b10243

65. Menke, S. M., Ran, N. A., Bazan, G. C., & Friend, R. H. (2018). Understanding Energy Loss in Organic Solar Cells: Toward a New Efficiency Regime. *Joule*, *2*(1), 25–35. https://doi.org/10.1016/j.joule.2017.09.020

66. Leblebici, S., Lee, J., Weber-Bargioni, A., & Ma, B. (2017). Dielectric Screening To Reduce Charge Transfer State Binding Energy in Organic Bulk Heterojunction Photovoltaics. *The Journal of Physical Chemistry C*, *121*(6), 3279–3285. https://doi.org/10.1021/acs.jpcc.6b12463

67. Bombile, J. H., Janik, M. J., & Milner, S. T. (2019). Energetics of exciton binding and dissociation in polythiophenes: A tight binding approach. *Physical Chemistry Chemical Physics*, *21*(22), 11999–12011. https://doi.org/10.1039/C9CP01116A

68. Zhu, L., Yi, Y., & Wei, Z. (2018). Exciton Binding Energies of Nonfullerene Small Molecule Acceptors: Implication for Exciton Dissociation Driving Forces in Organic Solar Cells. *The Journal of Physical Chemistry C*, *122*(39), 22309–22316. https://doi.org/10.1021/acs.jpcc.8b07197

69. Jiang, X., Yang, J., Karuthedath, S., Li, J., Lai, W., Li, C., Xiao, C., Ye, L., Ma, Z., Tang, Z., Laquai, F., & Li, W. (2020). Miscibility-Controlled Phase Separation in Double-Cable Conjugated Polymers for Single-Component Organic Solar Cells with Efficiencies over 8 %. *Angewandte Chemie*, *132*(48), 21867–21876. https://doi.org/10.1002/ange.202009272

70. Chen, K., Ma, R., Liu, T., Luo, Z., Xu, X., Wang, Q., Chen, Y., Xiao, Y., Lu, X., & Yan, H. (2020). Fluorinated pyrazine-based D–A conjugated polymers for efficient non-fullerene polymer solar cells. *Journal of Materials Chemistry A*, *8*(15), 7083–7089. https://doi.org/10.1039/D0TA00599A

71. Bin, H., Yang, Y., Peng, Z., Ye, L., Yao, J., Zhong, L., Sun, C., Gao, L., Huang, H., Li, X., Qiu, B., Xue, L., Zhang, Z.-G., Ade, H., & Li, Y. (2018). Effect of Alkylsilyl Side-Chain Structure on Photovoltaic Properties of Conjugated Polymer Donors. *Advanced Energy Materials*, *8*(8), 1702324. https://doi.org/10.1002/aenm.201702324

72. Yang, Y., Zhang, Z.-G., Bin, H., Chen, S., Gao, L., Xue, L., Yang, C., & Li, Y. (2016). Side-Chain Isomerization on an n-type Organic Semiconductor ITIC Acceptor Makes

11.77% High Efficiency Polymer Solar Cells. *Journal of the American Chemical Society*, *138*(45), 15011–15018. https://doi.org/10.1021/jacs.6b09110

73. Yan, C., Ma, R., Cai, G., Liu, T., Zhu, J., Wang, J., Li, Y., Huang, J., Luo, Z., Xiao, Y., Lu, X., Yang, T., Zhan, X., Yan, H., & Li, G. (2020). Reducing VOC loss via structure compatible and high lowest unoccupied molecular orbital nonfullerene acceptors for over 17%-efficiency ternary organic photovoltaics. *EcoMat*, *2*(4), e12061. https://doi.org/10.1002/eom2.12061

74. Muntwiler, M., Yang, Q., Tisdale, W. A., & Zhu, X.-Y. (2008). Coulomb Barrier for Charge Separation at an Organic Semiconductor Interface. *Physical Review Letters*, *101*(19), 196403. https://doi.org/10.1103/PhysRevLett.101.196403

75. Vandewal, K., Benduhn, J., & Nikolis, V. C. (2018). How to determine optical gaps and voltage losses in organic photovoltaic materials. *Sustainable Energy & Fuels*, *2*(3), 538–544. https://doi.org/10.1039/C7SE00601B

76. Li, H.-W., Guan, Z., Cheng, Y., Lui, T., Yang, Q., Lee, C.-S., Chen, S., & Tsang, S.-W. (2016). On the Study of Exciton Binding Energy with Direct Charge Generation in Photovoltaic Polymers. *Advanced Electronic Materials*, *2*(11), 1600200. https://doi.org/10.1002/aelm.201600200

77. Willems, R. E. M., Weijtens, C. H. L., Vries, X. de, Coehoorn, R., & Janssen, R. A. J. (2019). Relating Frontier Orbital Energies from Voltammetry and Photoelectron Spectroscopy to the Open-Circuit Voltage of Organic Solar Cells. *Advanced Energy Materials*, *9*(10), 1803677. https://doi.org/10.1002/aenm.201803677

78. Chandross, M., Mazumdar, S., Jeglinski, S., Wei, X., Vardeny, Z. V., Kwock, E. W., & Miller, T. M. (1994). Excitons in poly(*para* -phenylenevinylene). *Physical Review B*, *50*(19), 14702–14705. https://doi.org/10.1103/PhysRevB.50.14702

79. Hahn, T., Geiger, J., Blase, X., Duchemin, I., Niedzialek, D., Tscheuschner, S., Beljonne, D., Bässler, H., & Köhler, A. (2015). Does Excess Energy Assist Photogeneration in an Organic Low-Bandgap Solar Cell? *Advanced Functional Materials*, *25*(8), 1287–1295. https://doi.org/10.1002/adfm.201403784

80. Köhler, A., dos Santos, D. A., Beljonne, D., Shuai, Z., Brédas, J.-L., Holmes, A. B., Kraus, A., Müllen, K., & Friend, R. H. (1998). Charge separation in localized and delocalized electronic states in polymeric semiconductors. *Nature*, *392*(6679), 903–906. https://doi.org/10.1038/31901

81. Pichler, K., Halliday, D. A., Bradley, D. D. C., Burn, P. L., Friend, R. H., & Holmes, A. B. (1993). Optical spectroscopy of highly ordered poly(p-phenylene vinylene). *Journal of Physics: Condensed Matter*, *5*(38), 7155–7172. https://doi.org/10.1088/0953-8984/5/38/011

82. Yee, K. C., & Chance, R. R. (1978). Synthesis and properties of a new polydiacetylene: Poly[1,6-di(N-carbazolyl)-2,4-hexadiyne]. *Journal of Polymer Science: Polymer Physics Edition*, *16*(3), 431–441. https://doi.org/10.1002/pol.1978.180160307

83. van der Horst, J.-W., Bobbert, P. A., Michels, M. a. J., & Bässler, H. (2001). Calculation of excitonic properties of conjugated polymers using the Bethe–Salpeter equation. *The Journal of Chemical Physics*, *114*(15), 6950–6957. https://doi.org/10.1063/1.1356015

84. Engel, M., Kunze, F., Lupascu, D. C., Benson, N., & Schmechel, R. (2012). Reduced exciton binding energy in organic semiconductors: Tailoring the Coulomb interaction. *Physica Status Solidi (RRL) - Rapid Research Letters*, *6*(2), 68–70. https://doi.org/10.1002/pssr.201105488

85. Rand, B. P., Burk, D. P., & Forrest, S. R. (2007). Offset energies at organic semiconductor heterojunctions and their influence on the open-circuit voltage of thin-film solar cells. *Physical Review B*, *75*(11), 115327. https://doi.org/10.1103/PhysRevB.75.115327

86. Xu, X., Li, Z., Wang, J., Lin, B., Ma, W., Xia, Y., Andersson, M. R., Janssen, R. A. J., & Wang, E. (2018). High-performance all-polymer solar cells based on fluorinated naphthalene diimide acceptor polymers with fine-tuned crystallinity and enhanced dielectric constants. *Nano Energy*, *45*, 368–379. https://doi.org/10.1016/j.nanoen.2018.01.012

87. Duan, L., Zhang, Y., Yi, H., Haque, F., Xu, C., Wang, S., & Uddin, A. (2020). Thermal annealing dependent dielectric properties and energetic disorder in PffBT4T-2OD based organic solar cells. *Materials Science in Semiconductor Processing*, *105*, 104750. https://doi.org/10.1016/j.mssp.2019.104750

88. Roncali, J., & Grosu, I. (2019). The Dawn of Single Material Organic Solar Cells. *Advanced Science*, *6*(1), 1801026. https://doi.org/10.1002/advs.201801026

89. Inche Ibrahim, M. L., Ahmad, Z., Sulaiman, K., & Muniandy, S. V. (2014). Combined influence of carrier mobility and dielectric constant on the performance of organic

bulk heterojunction solar cells. *AIP Advances*, *4*(5), 057133. https://doi.org/10.1063/1.4881080

90. Koster, L. J. A., Shaheen, S. E., & Hummelen, J. C. (2012). Pathways to a New Efficiency Regime for Organic Solar Cells. *Advanced Energy Materials*, *2*(10), 1246–1253. https://doi.org/10.1002/aenm.201200103

91. Brebels, J., Manca, J. V., Lutsen, L., Vanderzande, D., & Maes, W. (2017). High dielectric constant conjugated materials for organic photovoltaics. *Journal of Materials Chemistry A*, *5*(46), 24037–24050. https://doi.org/10.1039/C7TA06808E

92. Zhang, X., Zhang, D., Zhou, Q., Wang, R., Zhou, J., Wang, J., Zhou, H., & Zhang, Y. (2019). Fluorination with an enlarged dielectric constant prompts charge separation and reduces bimolecular recombination in non-fullerene organic solar cells with a high fill factor and efficiency > 13%. *Nano Energy*, *56*, 494–501. https://doi.org/10.1016/j.nanoen.2018.11.067

93. Carsten, B., Szarko, J. M., Son, H. J., Wang, W., Lu, L., He, F., Rolczynski, B. S., Lou, S. J., Chen, L. X., & Yu, L. (2011). Examining the Effect of the Dipole Moment on Charge Separation in Donor–Acceptor Polymers for Organic Photovoltaic Applications. *Journal of the American Chemical Society*, *133*(50), 20468–20475. https://doi.org/10.1021/ja208642b

94. Knupfer, M. (2003). Exciton binding energies in organic semiconductors. *Applied Physics A*, *77*(5), 623–626. https://doi.org/10.1007/s00339-003-2182-9

95. Liu, F., Gu, Y., Shen, X., Ferdous, S., Wang, H.-W., & Russell, T. P. (2013). Characterization of the morphology of solution-processed bulk heterojunction organic

photovoltaics. *Progress in Polymer Science*, *38*(12), 1990–2052. https://doi.org/10.1016/j.progpolymsci.2013.07.010

96. Liu, J., Sun, Y., Gao, X., Xing, R., Zheng, L., Wu, S., Geng, Y., & Han, Y. (2011). Oriented Poly(3-hexylthiophene) Nanofibril with the π−π Stacking Growth Direction by Solvent Directional Evaporation. *Langmuir*, *27*(7), 4212–4219. https://doi.org/10.1021/la105109t

97. Liu, J., Arif, M., Zou, J., Khondaker, S. I., & Zhai, L. (2009). Controlling Poly(3-hexylthiophene) Crystal Dimension: Nanowhiskers and Nanoribbons. *Macromolecules*, *42*(24), 9390–9393. https://doi.org/10.1021/ma901955c

98. Carsten, B., Szarko, J. M., Lu, L., Son, H. J., He, F., Botros, Y. Y., Chen, L. X., & Yu, L. (2012). Mediating Solar Cell Performance by Controlling the Internal Dipole Change in Organic Photovoltaic Polymers. *Macromolecules*, *45*(16), 6390–6395. https://doi.org/10.1021/ma3011119

99. Ye, L., Zhao, W., Li, S., Mukherjee, S., Carpenter, J. H., Awartani, O., Jiao, X., Hou, J., & Ade, H. (2017). High-Efficiency Nonfullerene Organic Solar Cells: Critical Factors that Affect Complex Multi-Length Scale Morphology and Device Performance. *Advanced Energy Materials*, *7*(7), 1602000. https://doi.org/10.1002/aenm.201602000

100. Wang, L.-M., Li, Q., Liu, S., Cao, Z., Cai, Y.-P., Jiao, X., Lai, H., Xie, W., Zhan, X., & Zhu, T. (2020). Quantitative Determination of the Vertical Segregation and Molecular Ordering of PBDB-T/ITIC Blend Films with Solvent Additives. *ACS Applied Materials & Interfaces*, *12*(21), 24165–24173. https://doi.org/10.1021/acsami.0c02843

101. Boufflet, P., Bovo, G., Occhi, L., Yuan, H.-K., Fei, Z., Han, Y., Anthopoulos, T. D., Stavrinou, P. N., & Heeney, M. (2018). The Influence of Backbone Fluorination on the Dielectric Constant of Conjugated Polythiophenes. *Advanced Electronic Materials*, *4*(10), 1700375. https://doi.org/10.1002/aelm.201700375

102. Hughes, M. P., Rosenthal, K. D., Dasari, R. R., Luginbuhl, B. R., Yurash, B., Marder, S. R., & Nguyen, T.-Q. (2019). Charge Recombination Dynamics in Organic Photovoltaic Systems with Enhanced Dielectric Constant. *Advanced Functional Materials*, *29*(29), 1901269. https://doi.org/10.1002/adfm.201901269

103. Constantinou, I., Yi, X., Shewmon, N. T., Klump, E. D., Peng, C., Garakyaraghi, S., Lo, C. K., Reynolds, J. R., Castellano, F. N., & So, F. (2017). Effect of Polymer–Fullerene Interaction on the Dielectric Properties of the Blend. *Advanced Energy Materials*, *7*(13), 1601947. https://doi.org/10.1002/aenm.201601947

104. Li, Z., Xu, X., Zhang, W., Meng, X., Ma, W., Yartsev, A., Inganäs, O., Andersson, Mats. R., Janssen, R. A. J., & Wang, E. (2016). High Performance All-Polymer Solar Cells by Synergistic Effects of Fine-Tuned Crystallinity and Solvent Annealing. *Journal of the American Chemical Society*, *138*(34), 10935–10944. https://doi.org/10.1021/jacs.6b04822

105. Rueden, C. T., Schindelin, J., Hiner, M. C., DeZonia, B. E., Walter, A. E., Arena, E. T., & Eliceiri, K. W. (2017). ImageJ2: ImageJ for the next generation of scientific image data. *BMC Bioinformatics*, *18*(1), 529. https://doi.org/10.1186/s12859-017-1934-z

106. Mihailetchi, V. D., Koster, L. J. A., Hummelen, J. C., & Blom, P. W. M. (2004). Photocurrent Generation in Polymer-Fullerene Bulk Heterojunctions. *Physical Review Letters*, *93*(21), 216601. https://doi.org/10.1103/PhysRevLett.93.216601

107. Ye, L., Li, W., Guo, X., Zhang, M., & Ade, H. (2019). Polymer Side-Chain Variation Induces Microstructural Disparity in Nonfullerene Solar Cells. *Chemistry of Materials*, *31*(17), 6568–6577. https://doi.org/10.1021/acs.chemmater.9b00174